



저작자표시-비영리-변경금지 2.0 대한민국

이용자는 아래의 조건을 따르는 경우에 한하여 자유롭게

- 이 저작물을 복제, 배포, 전송, 전시, 공연 및 방송할 수 있습니다.

다음과 같은 조건을 따라야 합니다:



저작자표시. 귀하는 원저작자를 표시하여야 합니다.



비영리. 귀하는 이 저작물을 영리 목적으로 이용할 수 없습니다.



변경금지. 귀하는 이 저작물을 개작, 변형 또는 가공할 수 없습니다.

- 귀하는, 이 저작물의 재이용이나 배포의 경우, 이 저작물에 적용된 이용허락조건을 명확하게 나타내어야 합니다.
- 저작권자로부터 별도의 허가를 받으면 이러한 조건들은 적용되지 않습니다.

저작권법에 따른 이용자의 권리는 위의 내용에 의하여 영향을 받지 않습니다.

이것은 [이용허락규약\(Legal Code\)](#)을 이해하기 쉽게 요약한 것입니다.

[Disclaimer](#)

공학박사 학위논문

**Liquid Droplet Impingement
Erosion Mechanism of Low-Alloy
Steels in the Secondary Side of
Pressurized Water Reactors**

가압경수형 원자로 2차측 저합금강의
액적충돌침식 손상기구 연구

2015년 8월

서울대학교 대학원

에너지시스템공학부

남 원 창

Liquid Droplet Impingement Erosion Mechanism of Low-Alloy Steels in the Secondary Side of Pressurized Water Reactors

지도 교수 황 일 순

이 논문을 공학박사 학위논문으로 제출함
2015 년 7 월

서울대학교 대학원
에너지시스템공학부
남 원 창

남원창의 박사 학위논문을 인준함
2014 년 8 월

위 원 장 이 경 우 (인)

부위원장 황 일 순 (인)

위 원 이 인 형 (인)

위 원 한 병 찬 (인)

위 원 황 경 모 (인)

Abstract

Liquid Droplet Impingement Erosion Mechanism of Low-Alloy Steels in the Secondary Side of Pressurized Water Reactors

Nam, Won Chang

School of Energy Systems Engineering

The Graduate School

Seoul National University

Reliable operation of nuclear power plants (NPPs) is necessary for producing stable electricity and reducing the carbon emission. In this post-Fukushima era where the safety enhancement of NPPs has emerged as the most mandates, aging management of operating NPPs emerges as an imminent challenge. There are several material degradation issues relating to pressurized water reactors (PWRs) that constitute most of operated fleets in Korea. In order to ensure the safety of NPPs throughout a long-term operating period, the integrity of the structural materials within the NPPs must be secured.

Past studies on the material degradation issues have been focusing on the safety-critical problems which may arise with the structural materials constituting the primary pressure boundary (*i.e.* primary circuit) of PWRs. In contrast, issues with the secondary side of PWRs have received relatively insufficient attention. However, ruptures of piping systems in the secondary side of PWRs caused by the pipe wall-thinning phenomenon have persisted safety impact both within and outside Korea including losses of life and costly damages. Flow-accelerated corrosion (FAC) and liquid droplet impingement erosion (LDIE) have been identified as key causes of pipe wall-thinning

phenomenon. While significant understanding has been made for the former, little research has been conducted on the latter.

Interestingly, ruptures caused by LDIE have only recently been reported and no systematic research has been conducted on mechanisms or remedies. For long-term operation, it is thus essential to understand on the damage mechanism of LDIE. Difficulties in carrying out investigations arise from the fact that it is difficult to (i) simulate at a lab scale a phenomenon slowly develops in a time scale of over several decades; and (ii) identify the detailed micro-processes for such phenomenon due to the complex interactions among several key variables.

In this thesis, an accelerated test method has been developed and fundamental mechanisms as well as damage rates are examined for LDIE in simulated physico-chemical environments that are relevant to the secondary side of PWRs. In order to accelerate the LDIE phenomenon, experiments have been conducted under reducing conditions with; (i) the pH level is adjusted to a level lower than those of the secondary side of PWRs; and (ii) the velocity and size of water droplets are adjusted to levels higher than those of the secondary side of PWRs. LDIE experiments by controlling the pH level and velocity and size of water droplets under water chemistry conditions typical of actual plant have been made as a unique attempt to understand mechanisms.

A unique high temperature test apparatus has been developed in this thesis starting from the ASTM G-73-10 standard testing method which requires the control the velocity and size of water droplets. Water droplets having uniform density and size are sprayed through a nozzle and impinged upon specimens that are attached to the rim of rotating disc. Water droplets are produced by using chemically controlled water as a function of DO/DH concentrations, pH level and time.

Two types of typical low-alloy steels for PWRs have been studied, including A106 Gr.B (UNS K03006) and A335 P22 (UNS K21590). The latter with higher Cr contents has lower general corrosion rate than the former. High sulfur grade low-alloy steel, SUM24L (UNS G12144), is also tested to examine the effect of MnS inclusions. All tested materials have microstructure consisted of relatively equiaxed ferrite subgrains and lamellar pearlite regions.

Then, LDIE tests were conducted on test coupons by using the specially

developed apparatus. After measuring the accumulated mass-loss over testing time, it has been observed for all materials that: (i) there exists a transition point at which the damage rate thereafter increase significantly; (ii) prior to the transition point, damages tend to be initiated from a particular region of the surface of the specimen; and (iii) after the transition period, the test specimen, while under the same experimental conditions, displayed a higher damage rate than the rate displayed prior to the transition point.

By examining microstructure and nanostructure of damaged coupons, it has been observed that for all tested materials early damages tend to be mainly inflicted within the pearlite structure whereas the ferrite structure remained relatively intact. Microscopic observations of damaged area revealed that the LDIE phenomenon occurred in the following sequence: the selective dissolution of ferrite layers within the pearlite structure leaving cementite plate behind. The selective dissolution of ferrite has been previously reported to have been caused by a galvanic effect arising from the electrochemical disparity between alternating layers of cementite and ferrite, acting as the cathode and anode, respectively. Subsequent erosion by impinged water droplets of the cementite layers within such pearlite structure leads to the detachment of the top surface layer and reveal underlying layer with high roughness. Water droplet impingement on the roughened surface thereafter significantly increase momentum transfer and the erosion rate.

Similar behavior was observed with A335 P22. Microscopic observations of A335 P22 displayed the same phenomenon where damages were mainly inflicted on the pearlite structure and the ferrite structure remained relatively stable until a certain point in time, as well as the same sequence of events observed on A106 Gr.B.

Therefore, this research proposes a damage mechanism for liquid droplet impingement erosion (LDIE), an identified cause of the pipe wall-thinning phenomenon in the secondary side of PWRs, which is explained by the first step of corrosion-induced roughing of surface layer and the second step of erosion-induced material removal. The transition from the first to the second step occurred when the surface grains are removed.

Based on the results of this research, a bi-linear prediction model has been proposed, as functions of time, pH, and water droplet momentum to delineate

the corrosion-induced period and the erosion-dominating period. The model was applied to predict one known case of a field failure to fail that the developed model over-predict the damage rate and under-predict the failure time by about 30%, indicating a fair agreement.

Keywords: Liquid droplet impingement erosion, Low-alloy steel, PWR, Damage mechanism, Accelerating test method.

Student Number: 2005-31016

Table of Contents

Chapter 1.Introduction.....1

1.1	Background	1
1.2	Issues of material aging in the secondary side of PWRs	3
1.2.1	Overview of aging issues in PWRs.....	3
1.2.2	Pipe wall thinning of the secondary side of PWRs	6
1.2.3	Pipe wall thinning due to LDIE	10
1.3	Objectives	17

Chapter 2.Literature Review18

2.1	Erosion of low-alloy steel (LAS)	18
2.1.1	Theories of LDIE	18
2.1.2	Low-alloy steel (LAS)	20
2.1.3	Key variables.....	22
2.2	Water chemistry in PWR secondary side	23
2.2.1	pH.....	23
2.2.2	Dissolved oxygen (DO)	24
2.2.3	Temperature.....	24
2.2.4	Velocity	26

2.3	Previous models for liquid droplet impingement erosion (LDIE).....	33
2.3.1	Experimental models	33
2.3.2	Corrosion–erosion combined models	35
Chapter 3.Rationale and Approach.....		40
3.1	Problem statement.....	40
3.2	Goals	41
3.3	Approach.....	42
Chapter 4.Experimental Design and Procedure		44
4.1	Microstructure and chemistry of materials	44
4.2	Development of the LDIE accelerated test apparatus.....	50
4.3	Test matrix and test procedures.....	59
Chapter 5.Experimental Results.....		65
5.1	Analysis of experimental results	65
5.2	Microstructural evolution of damages	67
Chapter 6.Mechanism of LDIE Damage		77
6.1	Corrosion mechanism	77
6.2	Erosion mechanism	84
6.3	Microstructural damage propagation process	88

Chapter 7.LDIE Prediction Model	92
7.1 Semi-empirical model for pipe wall thinning	92
7.2 Model benchmark with field data	109
Chapter 8. Conclusions.....	114
8.1 Conclusions.....	114
8.2 Future work.....	118
References	119
Appendix	126
A1. Mass loss database of LDIE acceleration test.....	126
A2. Microstructure images for LDIE damaged specimens.....	128
초 록	131

List of Tables

Table 1.1 Chemical composition of materials of the failure cases in the secondary side of domestic PWRs[4].	14
Table 2.1 Key factors influencing LDIE of low-alloy steels	27
Table 4.1 Chemical composition and yield strength of LDIE test materials(wt.%)	47
Table 4.2 LDIE test matrix and the error of measurement (at 150 °C, less than 5 ppb of dissolved oxygen)	62
Table 7.1 Transition time, <i>t_{ce}</i> obtained from microstructure and mass loss data.....	100
Table 7.2 Field failure case-operation conditions and droplet properties[75].	111
Table 7.3 Field failure case-information of damaged material.	111
Table 7.4 Predicted results using a field failure case assuming the number density of impinging droplets as $1.86 \times 10^7 \text{ \#}/\text{cm}^2\text{hr}$	112

List of Figures

Figure 1.1 Material aging and degradation issues in the primary and secondary side of PWRs.	5
Figure 1.2 Diagram of the secondary cooling system of PWRs(HP-high pressure turbine, LP-low pressure turbine, FWST-feedwater storage tank, FWP-feedwater pump)[24].	12
Figure 1.3 Wall-thinning and leak failures occurred in domestic PWRs (as function of materials)[4].	13
Figure 1.4 Failure components by liquid droplet impingement erosion in the secondary side of PWRs-(a)Korean Unit Y #2, HP FW HTR to Re-heater, A106 Gr.B, (b) Korean Unit W #1, FW Re-heater, A234 WPB, (c) Belgium Tihange Unit #1, LP turbine casing, no information about material[4,5].	15
Figure 1.5 Phenomena identified ranking table (PIRT) for the structural material degradation mechanism of SSC in PWRs[13-15].	16
Figure 2.1 Classification of ferrous alloys[29].	28
Figure 2.2 Schematic illustration of erosion damage process by liquid droplet impingement in ductile materials-(a) initial stage of erosion (b) plastic deformation at grain boundaries (c) crack initiation by fatigue (d) erosion on surface (e) further eroded surface[31].	29
Figure 2.3 Microstructure of LDIE damaged specimen-(a) Type 403 martensitic stainless steel[28], (b) S15C carbon steel tested at 160 m/s of droplet velocity[31].	30

Figure 2.4 The environmental factor dependence on erosion-corrosion rate- (a) pH effect[41], (b) dissolved oxygen effect[39], (c) temperature effect[41], (d) flow velocity effect[41].31

Figure 2.5 Temperature dependence of single-phase flow-accelerated corrosion with ammonia at pH 9.0(C_{eq} is magnetite solubility and k is mass transfer coefficient)[42]. 32

Figure 2.6 Wall thinning rate due to liquid droplet impingement[52].36

Figure 2.7 Field failure case-(a) schematic of damage scenario, (b) inner surface of damaged pipe, (c) microstructure of damaged surface, (d) cross-sectional image (A234 WPB, operated about 20 yr. at 138°C)[4].37

Figure 2.8 Corrosion product particle mean circular diameter distribution of high pressure drains and feedwater at South Texas Project Unit 1[61].38

Figure 2.9 Flow accelerated corrosion model-(1) production of soluble ferrous ions at the iron/magnetite interface, (2) diffusion of soluble ferrous ions through porous oxide layer, (3) dissolution of magnetite at the oxide/water interface, (4) transfer of the ferrous ions into the bulk water across diffusion boundary[68].39

Figure 3.1 Diagram for LDIE mechanistic study43

Figure 4.1 Photomicrographs of 2% nital etched test materials; (a) A106 Gr.B, (b) A334 P22, and (c) SUM24L.48

Figure 4.2 Nanoscale photomicrographs of test materials revealing

cementite layers left as a result of dissolution of ferrite layers in between (FE-SEM).	49
Figure 4.3 The schematic of LDIE test apparatus based on ASTM G73-10 standard method.....	55
Figure 4.4 Piping and instrument diagram (P&ID) for balancing water chemistry and recirculation	56
Figure 4.5 Droplet characteristics measurement-(a) schematic of droplet size measurement, (b) droplet size measurement system by using DSLR and strobe light.....	57
Figure 4.6 Droplet diameter and distribution-(a) Sauter mean diameter(SMD) is 613 μm for Nozzle size(600 μm), (b) Sauter mean diameter(SMD) is 379 μm for Nozzle size(600 μm). ...	58
Figure 4.7 pH and electrochemical potential under test conditions calculated by HSC chemistry[70].	63
Figure 4.8 Magnetite solubility as functions of temperature and pH[69].	64
Figure 5.1 Mass loss of LAS as a function of pH.	69
Figure 5.2 Mass loss of LAS as a function of droplet velocity.	70
Figure 5.3 Mass loss of LAS as a function of droplet diameter.	71
Figure 5.4 Long-term experiment for up to 200 hr.	72
Figure 5.5 Time dependence of microstructures of A106 Gr.B (pH- 4, V-80m/s, d-700 μm , T-150 $^{\circ}\text{C}$, x1000 magnification)	73
Figure 5.6 Cross-sectional microstructure of a field failure specimen –(a) MnS stringer in both optical microscope and EDS), (b) Carbon rich phase near damaged surface	74
Figure 5.7 Initiation stage of LDIE damage-dependence of sulfur	

contents	75
Figure 5.8 Sulfur rich area obtained by (a) sulfur print for A106 Gr.B, and (b) EDS for SUM24L.	76
Figure 6.1 Initiation of LDIE damage(A106 Gr.B, pH 4, droplet velocity 80 m/s, droplet diameter 700 μm)-(a) cavities due to iron dissolution on pearlite, (b) the lamellar structure of cementite layers.....	80
Figure 6.2 Initiation of damage(A106 Gr.B, pH 4, droplet velocity 80 m/s, droplet diameter 700 μm)-(a) pearlite corrosion and revealed grain boundary, (b) ferrite-pearlite grain boundary damage.	81
Figure 6.3 Local damage initiation(A106 Gr.B, pH 4, droplet velocity 80 m/s, droplet diameter 700 μm)-(a) chunks of pearlite fell out of a pearlite region, (b) the lamellar structure teared by impinged droplets.	82
Figure 6.4 Local damage initiation(A106 Gr.B, pH 4, droplet velocity 80 m/s, droplet diameter 700 μm)-(a) damage path into the pearlite, (b) delamination of pearlite and ferrite-pearlite boundary damage (FIB).	83
Figure 6.5 Cross-sectional investigation of the damaged specimen during transition period.....	86
Figure 6.6 Cross-sectional investigation of the damaged specimen during stable-loss period.	87
Figure 6.7 The schematic of sequence of events and damage mechanism.	90
Figure 6.8 Reproducibility by a re-polish test.	91

Figure 7.1 Critical mass loss-(a) critical mass for A106 Gr.B(black square for 400 micrometer-droplet size, red circle for 600 micrometer-droplet size), (b) critical mass for A335 P22(black square for 400 micrometer-droplet size, red circle for 600 micrometer-droplet size).	101
Figure 7.2 Calculated transition time-(a) transition time as determined by the critical mass, (b) transition time as a function of pH.	102
Figure 7.3 Regression results and relationship between the mass loss rate and the key LDIE factors including the magnetite solubility C_e , the droplet velocity, V and the droplet diameter, d -(a) initiation stage, (b) stable-loss stage(after transition time).	103
Figure 7.4 Comparison of measured data and the Sanchez-Caldera model(for A106 Gr.B)- (a) initiation stage, (b) stable-loss stage(after transition time).	104
Figure 7.5 Comparison of measured data and the Sanchez-Caldera model for all test materials including A106 Gr.B, A335P22, and SUM24L -(a) initiation stage, (b) stable-loss stage(after transition time).	105
Figure 7.6 Material dependence of corrosion rate-(a) corrosion rate as a function of carbon content in steels[74], (b) Influence of Cr+Mo content on erosion-corrosion according to the experiments of KWU[43].....	106
Figure 7.7 Mass loss rate of LAS as a function of alloying contents-(a) carbon contents, (b) Cr and Mo contents.....	107

Figure 7.8 The schematic of developed model which is a bi-linear model including the corrosion-dominant initiation stage and the erosion-dominant stable-loss stage.108

Figure 7.9 Field failure case-(a) schematic of the damaged section, (b) photograph of the damaged area[4]..... 110

Figure 7.10 Comparison of the failure time and the model prediction result that is equal to 65%(about 12 yrs.) of the field failure time..... 113

Chapter 1. Introduction

1.1 Background

Both developed and developing countries are confronted with reducing carbon emission which is the main cause of global warming. For expanding energy supply to fulfill both needs of procuring a stable source of electricity and reducing the carbon emission level, massive, inexpensive, and low-carbon energy is needed. As a solution to meet the required demands, the electricity generated by nuclear power plants (NPPs) is an effective way.

Concerns with aged nuclear power plants are growing especially after the Fukushima accident in 2011. For the safe operation of nuclear power plants, degradation of structural materials should be adequately managed. As a plant gets older, a reduction in safety margins may occur with aging of structural materials. Recently, systematic approaches for the management of materials degradation are emphasized, so that mitigation, monitoring, and repair actions can be proactively developed, assessed, and implemented before the degradation process adversely impacts structural integrity[1].

The failure modes of structural materials are diverse, complex and persistent, depending on location and design. However, understanding the mechanisms of material degradation is a key for developing remedial measures needed for reliable operation of the NPPs. In this thesis, it is aimed that liquid droplet impingement erosion (LDIE) in the secondary side of PWRs is explored.

For the primary circuit including the reactor vessel, several key mechanisms have been identified. Irradiation effect on materials must be considered for high-fluence areas. Major consequences include conspicuously swelling, embrittlement, and radiation induced segregation. Thermo-chemo-mechanical effects including fatigue and stress corrosion cracking (SCC) must also be examined. Corrosion takes many forms of degradation in both primary circuit and the secondary system of PWRs.

In the secondary systems of a PWR, corrosion occurs in diverse. Understanding the various modes of corrosion and hence formulating mitigation strategies are important technical challenges to long-term operations of PWRs. Numerous failures in the secondary system have been reported as corrosion problems in lines for the extraction of steam, casing of turbines, and lines for moisture separation etc.

The propensity of secondary system components to corrosion is due to the fact that most materials are made of low-alloy steels or carbon steels, unlike the case of the primary systems. The pipe wall thinning in the secondary system by chemical, mechanical and/or chemo-mechanical synergistic actions have led to an increasing interest to this thesis. In the next section, material degradation in the secondary system is examined in further details.

1.2 Issues of material aging in the secondary side of PWRs

1.2.1 Overview of aging issues in PWRs

Aging degradation of systems, structures, and components (SSCs) in NPPs is defined as the cumulative degradation that occurs with the passage of time that can, if unchecked, lead to a loss of function and/or reliability[2]. Aging degradation results from a variety of physical, or chemical mechanisms such as creep, fatigue, embrittlement, wear, erosion, corrosion, and oxidation. These aging mechanisms act on SSCs in NPP operation environment including high temperature and pressure, radiation, reactive chemicals, and synergistic effects.

Figure 1.1 summarizes the key aging phenomena occurring at PWRs. In terms of plant safety, the reactor pressure vessel (RPV) is the most critical pressure boundary component in the PWRs. Neutron irradiation of RPV can produce several types of microstructural changes, which include precipitates, micro-voids, and dislocation loops. The radiation-induced microstructural changes cause an increase in the yield and ultimate tensile strengths and a decrease in the ductility and fracture toughness.

Major components within the primary systems such as steam generator (SG), pressurizer (PZR), reactor coolant system (RCS) piping, and control rod driving system (CRDM) nozzle are affected by stress corrosion cracking (SCC) which characterized by a long initiation time and crack growth along

the grain boundaries or phase interfaces of austenitic materials[3].

SG performs as a heat exchanger converting water into steam and a pressure boundary between the primary circuit and the secondary side of PWRs. SG tubes made by Alloy 600 suffered from SCC in both primary and secondary side. To reduce SCC susceptibility, Alloy 600 has been replaced by Alloy 690 having more Cr content to better corrosion resistance.

A surge line connects the pressurizer (PZR) to the hot leg, while a spray line connects it to the cold leg. The PZR shells are subject to fatigue damage caused by plant operation transients, water level changes, sloshing, and spray impact and so on. The surge line and spray nozzle connections to the PZR vessel are subjected to thermal fatigue loads caused by in-surges and out-surges, flow stratification in the surge and spray line piping , and the plant heat-ups and cool-downs.

SCC is also an important degradation issue for reactor coolant system (RCS) piping including hot and cold leg pipes. The weld regions of RCS piping are vulnerable to SCC. Reactor coolant pump (RCP) bodies are subjected to thermal and mechanical fatigue damage caused by the system transients and pump vibrations.

The main aging degradation mechanisms affecting the secondary systems include corrosion and erosion. Especially, a flow-accelerated corrosion affects pipe wall thinning of carbon steel piping and fitting carrying single-phase water, subcooled feed-water, and wet steam.

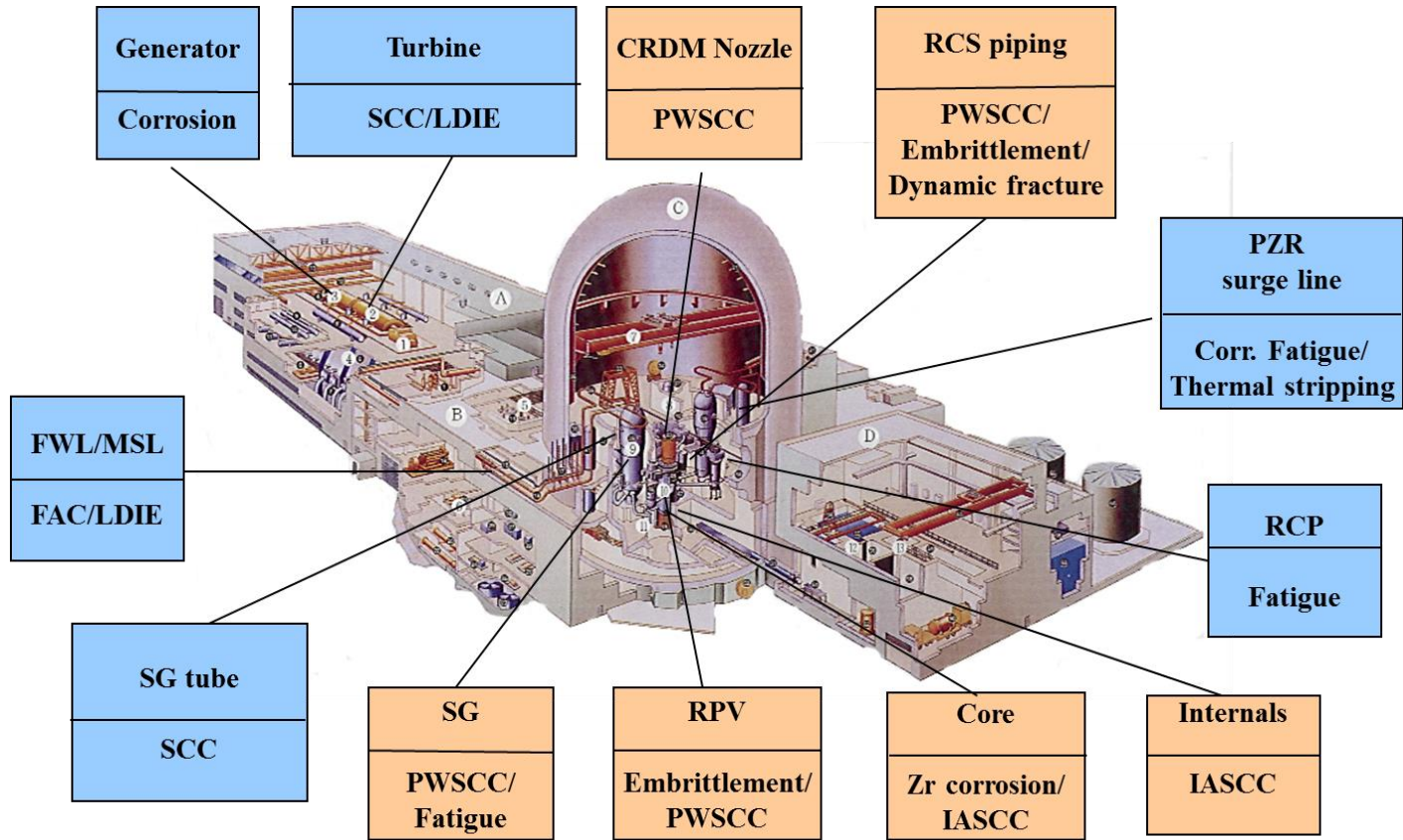


Figure 1.1 Material aging and degradation issues in the primary and secondary side of PWRs.

1.2.2 Pipe wall thinning of the secondary side of PWRs

Past research on the material aging degradation issue has been focusing on the possible problems which may arise with respect to the structural materials located within the primary pressure boundary (*i.e.* primary circuit). However, the secondary side of PWRs, including feed-water systems and steam supply systems, are also important to assure the safety of NPPs. Especially, a loss of feed-water is an event that activates and challenges safety-related systems, and several aging-related feed-water piping failures have been recently occurred within and outside Korea[4,5]. Failure of high-energy piping, such as the feed-water system piping, can also result in complex challenges to the plant operating staff because of potential interactions of the high-energy steam and water with other systems such as the electrical distribution, fire protection, and security systems. Catastrophic failure of any high-energy piping also presents a safety problem for plant personnel.

As shown Figure 1.2, in the secondary systems for PWRs, steam is converted from the SGs in the primary systems to electrical power. Steam from the SG is supplied to the turbine that drives a generator connected to the electric grid for electricity distribution. From the turbine, exhaust steam-water mixture is cooled and condensed in a condenser before being returned into the SG again.

Specifically, the turbine system is divided into high- and low-pressure turbines. A small portion of the steam from the high-pressure turbine is extracted to the feed-water heaters; the remainder is exhausted to moisture

separator re-heater (MSR) with additional extractions to feed-water heater systems.

In the MSR, moisture is mechanically separated from the exhaust steam and the improved steam is then superheated before entering the low-pressure turbines. Therefore MSR deals with steam flow containing liquid droplets both are flowing at high speed. Liquid droplets contain lower concentration of ammonia compared with steam, hence leading to a pH decrease. Pipes in MSR are made of low-alloy steels that are vulnerable to corrosion and erosion in the operation environment.

One of the most important degradation mechanisms is known as flow-accelerated corrosion (FAC) which is a process whereby the inadequately protective iron oxide layer (mostly magnetite, Fe_3O_4) on carbon or low-alloy steels dissolve into a fast stream of flowing water. The damage caused by FAC is higher than the damage attributed to general corrosion or erosion alone.

Various erosion mechanisms also affect the systems of the secondary side of PWRs where liquid droplets and/or dust particles move at high speed with normal steam flow or by cavitation. There are three types of erosion mechanisms that can occur in the steam and feed-water systems; namely, cavitation erosion (CE), solid particle erosion (SPE), and liquid droplet impingement erosion (LDIE).

CE damage may occur when there is a flowing liquid stream that experiences a sudden pressure drop (*i.e.* the difference between up- and downstream pressures) followed by a pressure recovery. Such a sudden pressure drop can occur in valve internals where the flow has to accelerate through a

small area. As the fluid moves through the limited area, the fluid velocity increases and the pressure decreases. If the local pressure passes below the vapor pressure at the water temperature, then small bubbles formed. When the down-stream pressure rises above the vapor pressure, these bubbles collapse. The collapse of the bubbles causes high local pressures and water jet velocities, accompanied with noise and vibration. If the collapsing bubbles are close enough to a solid surface, mechanical damage to that surface will result. To prevent CE damage, a sudden pressure gradient should be avoided by design and operation procedures.

SPE occurs when particles carried by a stream of water or water-steam mixture impinge against structural material causing the structural material such as a piping, casing and/or valve to deform or remove the impinged surface of that. SPE has been found in the SG blowdown system of PWRs where accumulated sludge retained[5]. Fundamental studies on SPE mechanism have been conducted extensively on material response against the impinging particles in terms of impact angles and forces. Finne[6] clearly identified material removal mechanisms for both ductile and brittle material. The removal occurs by a process of displacement and cutting on ductile material, while the removal in brittle material is achieved through interaction and propagation of cracks. In limited explanation about inaccurate prediction of ductile material erosion at normal impact angles, Bitter[7-8] proposed an erosion model combining both deformation and cutting erosion. In Bitter's model, the two erosion mechanisms occur simultaneously in ductile materials. Particle size can affect the critical Kose[9] stated that the size of the erodent

particle has little or no effect on the erosion rate of ductile materials as long as the particle size is above about 100 microns, however, the erosion rate decreases rapidly with decreasing particle size below 100 microns[9,10].

LDIE is defined as a progressive loss of original material from a solid surface due to continued exposure to impacts by liquid drops or jets[11]. As a practical situation, LDIE in steam turbine internals has been studied since the 1920s[12-14]. As a result of exposure in repetitive attack by small liquid droplets, the droplets cause damage to a turbine blade resulting in surfaces characterized by high roughness and porosity. Most of the steam turbine erosion problems have been managed through improved designs, materials, and operation conditions. Meanwhile, LDIE occurs when two-phase stream (i.e. water-steam mixture in the secondary side of PWRs) is subjected to a high-pressure drop (e.g. across an orifice on a line to the condenser). When this occurs, there is an increase of the water droplet velocity which results in damage on an impacting surface of materials.

LDIE, CE, and SPE can be managed by improving operation conditions and geometrical designs as well as materials. Prediction models to predict CE and SPE have been developed and the model was adapted to the operating PWRs[14-15]. As mentioned earlier, the components such as valves, pump impellers should be designed by reducing hydrodynamic pressure gradients and designing to avoid pressure drops below the vapor pressure of the water. However, prediction models for LDIE are not available[17-19].

Recently, pipe wall thinning and subsequent leakages due to LDIE have been reported from the operating PWRs at increased frequency[4,5, and 15].

As shown in Figure 1.3 and Table 1.1, carbon or low-alloy steel piping and fitting was damaged by the LDIE, even though a droplet velocity according to estimating operation conditions is relatively lower than other LDIE cases. It presents safety problems to operating crew who can be exposed to high pressure and temperature steam. From the field experiences and previous work, an adequate mechanism to explain LDIE phenomenon in a piping environment has not been established, whereas CE, SPE can be managed by adequate prevention techniques.

1.2.3 Pipe wall thinning due to LDIE

LDIE phenomenon is responsible for localized pipe wall thinning by high speed impact of liquid droplets in locations, such as lines for extraction of steam, feed water re-heater, moisture separator re-heater, and casings of turbines in the secondary side of PWRs[4,5,20-22]. Many leaks caused by LDIE in which relatively low-quality steam-water mixture passing through are frequently observed in the operating PWRs(Figure 1.4). In all cases, local wall thinning failures at orifice, elbow, and tee junction show clear geometrical dependence in which flow conditions are prone to liquid droplet impingement. Because of the paucity of information on the operating conditions and droplet characteristics in the LDIE damaged region, LDIE damage has not been well characterized to understand detail mechanism.

Figure 1.5 shows the phenomena identified ranking table (PIRT) about the relationship between our knowledge basis and the susceptibility recognizing

in operating PWRs[1,15,and 23]. Compared with other damage mechanisms, the knowledge level of LDIE is relatively low, while the degradation susceptibility in PWR is above the average level. Even worse, there is no prediction model to manage LDIE. Plant outages due to LDIE have been about 20 days per year[4].

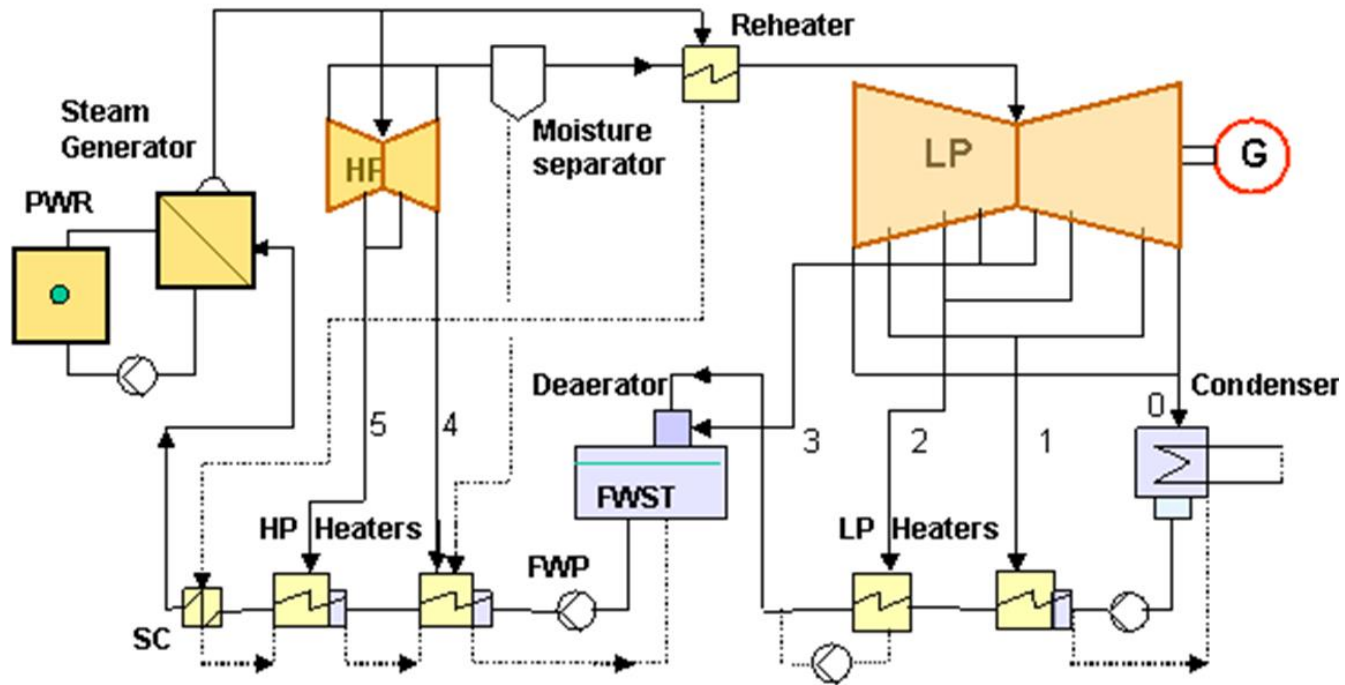


Figure 1.2 Diagram of the secondary cooling system of PWRs(HP-high pressure turbine, LP-low pressure turbine, FWST-feedwater storage tank, FWP-feedwater pump)[24].

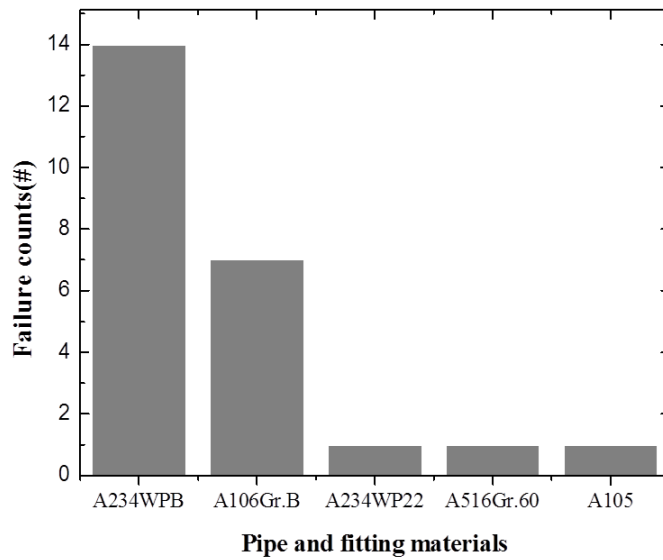


Figure 1.3 Wall-thinning and leak failures occurred in domestic PWRs (as function of materials)[4].

Table 1.1 Chemical composition of materials of the failure cases in the secondary side of domestic PWRs[4].

Material	Chemical composition, wt.%									
	C	Mn	P	S	Si	Cr	Mo	Ni	Cu	Others
A234 WPB	0.30 max.	0.29- 1.06	0.050 max.	0.058 max.	0.10 min.	0.40 max	0.15 max.	0.40 max.	0.40 max.	V-0.08max.
A106 Gr.B	0.30 max.	0.29- 1.06	0.035 max.	0.035 max.	0.10 max.	0.40 max.	0.15 max.	0.40 max.	-	V-0.08max.
A234 WP22	0.05- 0.15	0.30- 0.60	0.040 mx.	0.040 max.	0.50 max.	1.90- 2.60	0.87- 1.13	-	-	-
A516 Gr.60	0.25 max.	0.60- 1.20	0.035 max.	0.035 max.	0.15- 0.40	-	-	-	-	-
A105	0.35 max.	0.60- 1.05	0.035 max.	0.040 max.	0.01- 0.35	0.30 max.	0.12 max.	0.40 max.	0.40 max.	V-0.08max. Nb-0.02max.



(a) Korean Unit Y #2



(b) Korean Unit W #1



(c) Belgium Tihange Unit #1

Figure 1.4 Failure components by liquid droplet impingement erosion in the secondary side of PWRs-(a)Korean Unit Y #2, HP FW HTR to Re-heater, A106 Gr.B, (b) Korean Unit W #1, FW Re-heater, A234 WPB, (c) Belgium Tihange Unit #1, LP turbine casing, no information about material[4,5].

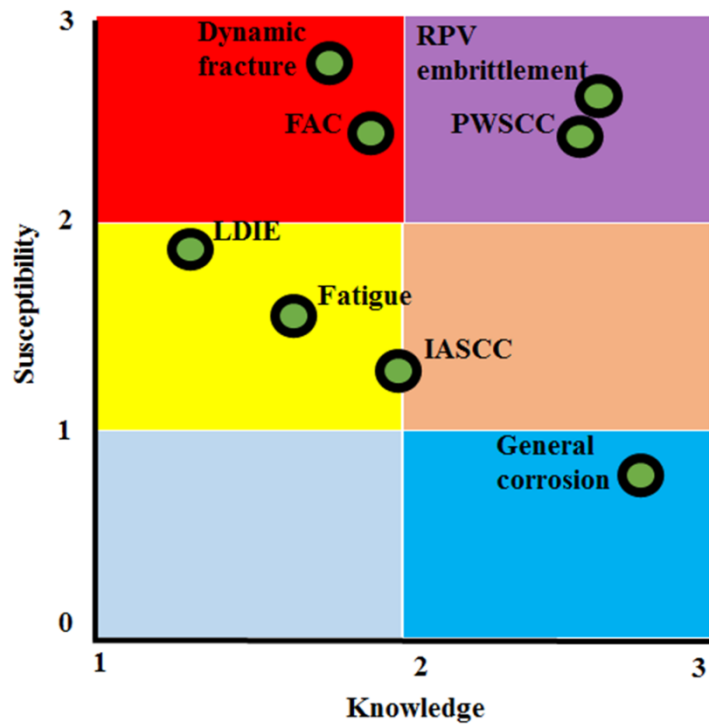


Figure 1.5 Phenomena identified ranking table (PIRT) for the structural material degradation mechanism of SSC in PWRs[13-15].

1.3 Objectives

The current state of poor understanding of LDIE mechanisms and the lack of prediction models was becoming a growing issue as increasing the failures of LDIE in the secondary side of PWRs. To predict and control LDIE damages, the first objective of this thesis is the fundamental understanding of LDIE mechanism. As the second objective, key variables affecting the LDIE damage mechanism will be identified. The last objective is to develop a semi-empirical prediction model. Acceleration experiments will be carried out by developing a delineated apparatus. The apparatus to be developed should be simulating LDIE damage under the same and/or accelerated conditions of the secondary side of PWRs. The test results will be analyzed to identify damage mechanism and to develop a prediction model.

Chapter 2. Literature Review

2.1 Erosion of low-alloy steel (LAS)

2.1.1 Theories of LDIE

LDIE has been defined earlier as continuing material loss of a solid target material due to continued exposure to impacts by liquid drops.[11] The LDIE damage results from repeated impacts by split liquid drops. The impact effect of the split droplets is that the droplets give rise to impulsive contact pressures on the solid target material, higher than those caused by steady flows [25] Thus, the endurance limit and even the yield strength of the target material can easily be exceeded, thereby causing damage by purely mechanical interactions. In some circumstances, the damage can also be accelerated by conjoint chemical reaction.

At sufficiently high impact velocities of liquid droplets, solid target material can be damaged by mechanical force. Much of what is currently known about the liquid/solid interactions in liquid impingement has been determined through laboratory experiments and analytical modeling based on single droplet impact.

The high velocity impact of a liquid drop on a solid surface produces two effects that result in damage to that surface: high contact pressure, which is generated in the area of the impact, and subsequent liquid jetting flow along the surface, radiating out from the impact area.[26] An approximation of the average impact pressure before radial outflow initiates, is the one-dimensional

water-hammer pressure which is the pressure generated in the impact of an infinite flat liquid surface against an infinite flat rigid surface. This impact or shock pressure, P (Pa) can be defined as[26]

$$P = \rho CV \quad \text{Eq. (2.1)}$$

where ρ is the liquid density, kg/m^3 , C is the shock wave velocity in the liquid, m/s , and V is the impact velocity, m/s . For practical impact velocities, this can be approximated by[27]

$$P = \rho C_0 V (1 + kV/C_0) \quad \text{Eq. (2.2)}$$

where C_0 is the acoustic velocity of the liquid, m/s , and k is 2 for water, a dimensionless value.

The above mathematical expression is an ideal case to understand how the external stressors affect the material damage. In actual situation, the liquid/solid interaction is more complicated, because of the roughness of the impacting droplets and the elastic and plastic deformations of the solid surfaces. LDIE in the late stages is characterized by a surface that appears jagged, composed of sharp peaks and pits. If shallow pits are formed, subsequent material loss occurs preferentially in the pits and continues to deepen them[28].

2.1.2 Low-alloy steel (LAS)

The leakage due to wall-thinning by LDIE has been reported from the operating PWRs, where low-alloy steels (LASs) are generally used for the piping and fitting materials in the secondary side. This thesis is focused on LDIE damages to LASs. Figure 2.1 shows how steels are classified. Generally, the carbon and low-alloy steels come under classification system based on composition. The American Iron and Steel Institute (AISI) defines carbon steel has no requirement of minimum contents of alloying elements such as chrome, cobalt, niobium, molybdenum and so on. The alloying elements are usually added to steels to obtain a desired alloying effect[29]. The total alloying elements of LASs do not exceed 8%.

As described in the previous section, the metal surface subjected to repeated impacts of liquid droplets become deformed and hardened. In ductile materials, single droplet impact may produce a central depression, with a ring of plastic deformation around it where jetting outflow by a tearing action[30].

With less intense but repeated impacts, the material loss may occur through propagation of fatigue-like cracks that eventually yield to release erosion fragments. Figure 2.2 illustrates schematically the progress of erosion damage in ductile materials under repeated droplet impingements[31]. Figure 2.2 (a) corresponds to the initial stage of erosion. The original surface is repeatedly exposed to liquid impingement and plastic deformation of the material surface occurs by shock waves of the impingement. Since the impingement repeatedly acts on the deformed area, the area gradually expands,

and the deformation accumulates at crystal grain boundaries. Since the material surface is plastically deformed, then asperities appear at the grain boundaries as shown in Figure 2.2 (b). These asperities produce a step relative to the adjacent grain with less plastic deformation and cause a high stress concentration, resulting in fatigue crack initiation as shown in Figure 2.2 (c). Figure 2.2 (d) shows that erosion easily occurs at crack initiation sites. Figure 2.2 (e) shows a further eroded surface.

Hobbs, Baker, and Heymann tested various materials to specify the erosion resistance of LDIE[17,32,and 33]. In the absence of any widely accepted, and physically consistent model for the LDIE, it is difficult to specify key independent variables. However, an attempt to quantify a normalized index in terms of the ratio of volume loss rates between a material and a reference material has been done. ASTM method G40[11] defines a normalized erosion resistance which is the ratio of the volume loss rate of a test material to the volume loss of a specified reference material. In ASM handbook[28], the reference material is austenitic stainless steel having Vickers hardness HV of 170. The erosion resistance of LAS was not quantitatively characterized but arrived to be comparable with carbon steel or cast iron if contents of chrome and molybdenum which are similar. Hardness of materials is known as a strong factor influencing erosion resistance[32]. High hardness materials tend to be more resistible to LDIE.

2.1.3 Key variables

There are several key variables influencing LDIE. They include droplet velocity, angle, and droplet size as well as material hardness[25-35]. There are summarized in Table 2.1. In brief, the LDIE rate increases as the velocity increases. It was said that the erosion rate is proportional to the n-th power of impact velocity[32-34].

The normal component of the impact velocity governs the rate of LDIE damage[35]. There appears to be a droplet size effect, with the smaller droplets causing less damage than larger droplets, when the total amount of droplets is the same in both cases. There is evidence that the droplet size effect becomes more pronounced toward lower velocities and smaller droplet sizes[8]. While several physical explanations for a size effect have been suggested, none has been proven as yet[36].

2.2 Water chemistry in PWR secondary side

The objective of controlling secondary side water chemistry in PWR is to minimize corrosion damage and thereby to enhance the reliability and economic performance of secondary systems that are constructed of LAS. In past studies on LDIE, the chemical environment did not reflect on the test results systematically. The water chemistry can determine the formation of protective oxides or dissolution of precipitates into the water.

The chemical effects on LDIE are not well understood. Nevertheless, it is widely accepted that three important parameters influencing the occurrence and rate of corrosion in flowing water are as follows: pH, dissolved oxygen (DO), and temperature[37-43].

2.2.1 pH

The pH is a factor that influences the solubility of LAS in water. The solubility is often correlated with corrosion rates. In the secondary side of PWRs, to minimize corrosion products which can be a result of wall thinning of structural materials and be sludge causing erosion problems, the pH maintain at a high value near 9[37].

However, many of the field data show that the failure time, at which total wall loss usually reaches full thickness, takes more than several decades.[4] Expecting an experiment with same condition of operating PWRs and supposing the corrosion effect affecting LDIE, the simulated damage time will take very long time as much as it takes in the actual condition. To accelerate

the LDIE damage simulation, the pH level can be lowered to increase the solubility and the corrosion rate of LAS.

2.2.2 Dissolved oxygen (DO)

Dissolved oxygen (DO) in water in the secondary side of PWRs is not specified not to exceed 5 ppb.[38] At the low DO condition, LAS surface develops magnetite layer.[39] The investigation of Brush and Pearl[38] on low carbon steel on temperature between 10 to 200°C, showed that an increase in the DO from 20 to 200 ppb decreases the corrosion-induced erosion rate by a factor of 10. The reason for this decrease in the rate has been explained by the passivation with hematite layer that is more protective than magnetite.[39] Passivity breakdown would be accompanied by severe localized corrosion, called pitting.[40] However, high DO is detrimental to SG tubes.[2]

2.2.3 Temperature

Corrosion rate of LAS in the secondary water changes with temperature. Figure 2.4 (c) shows that for the steel specimens from the corrosion test with a flowing water condition, there is a temperature at which the wear rate reaches a maximum value[41]. The critical temperature usually lies close to 150°C. Bouchacourt[42] explained the bell shape curve for temperature dependence of single-phase FAC. The FAC rate is controlled by oxide dissolution kinetics

at low temperatures and by mass transfer limitations at high temperatures as shown in Figure 2.5. The reason for this behavior is believed to be due to the competing behavior of two mechanisms in the temperature range between 100 to 250°C as follows. The solubility of the oxide layer decreases with increasing temperature above 150°C and the flow-accelerated corrosion is mass transfer controlled. The kinetics of the dissolution rate increases with increasing temperature below 150°C and the flow-accelerated corrosion is partially kinetics controlled. The pH of water in hot condition decreases with temperature.

At a low temperature the generation of ferrous ions is slow. As the temperature increases, more ferrous ions are generated. Thus there are more ferrous ions that can be carried away into the water flow. When temperature increases considerably, the conversion into magnetite is very fast. It tends to form a more protective film (i.e. less porous film), even the magnetite is known as having a porous structure, which leaves only a few ferrous ions to be removed by the water flow. As a result, the corrosion rate decreases in the range above the critical temperature.

The influence of temperature on corrosion rates is important from the point of view of controlling corrosion-induced erosion. In order to provide guidance for latent materials which can be easily damaged by LDIE in the secondary side of PWRs, it is necessary to estimate the effect on LAS in the range of temperatures near the critical temperature.

2.2.4 Velocity

The velocity of water increases the corrosion rate. Dissolved ferrous ion of LAS can be easily moved into the water by mass transfer process at the oxide-water interface. As the velocity increase, the mass transfer process is more active. Heitmann and Kastner found that the corrosion rate in flowing water is proportional to the mass transfer coefficient[43].

Table 2.1 Key factors influencing LDIE of low-alloy steels

Factors	Description	Discussion	Importance
Liquid/Solid interaction(A)			
A.1. Droplet velocity	- Erosion rate can be affected by impinging droplet velocity. -Usually proportional to velocity the velocity to the n-th order.	-It can be important in both erosion and corrosion phenomena[32-34].	High
A.2. Droplet diameter	-As the impact angle decreases, the erosion rate decreases.	-The maximum damage occurs at 90o of incident angle[35].	High
A.3 Impact angle	-Erosion rate is proportional to droplet size.	-Not only size effect but the number density of impinging droplets[28].	Middle
A.4 Corrosion factors	-In flow condition, max. corrosion rate occurs at 150°C. -pH can accelerate the corrosion rate. -Dissolved oxygen(DO) is maintained less than 5ppb in the secondary side of PWRs.	-There is little effort to consider corrosion factors.	High
Material response(B)			
B.1. Erosion resistance	-Hardness, Erosion resistance, and microstructure are important.	-The pipe and fitting materials of the secondary side of PWRs are carbon and low-alloy steels[4].	High

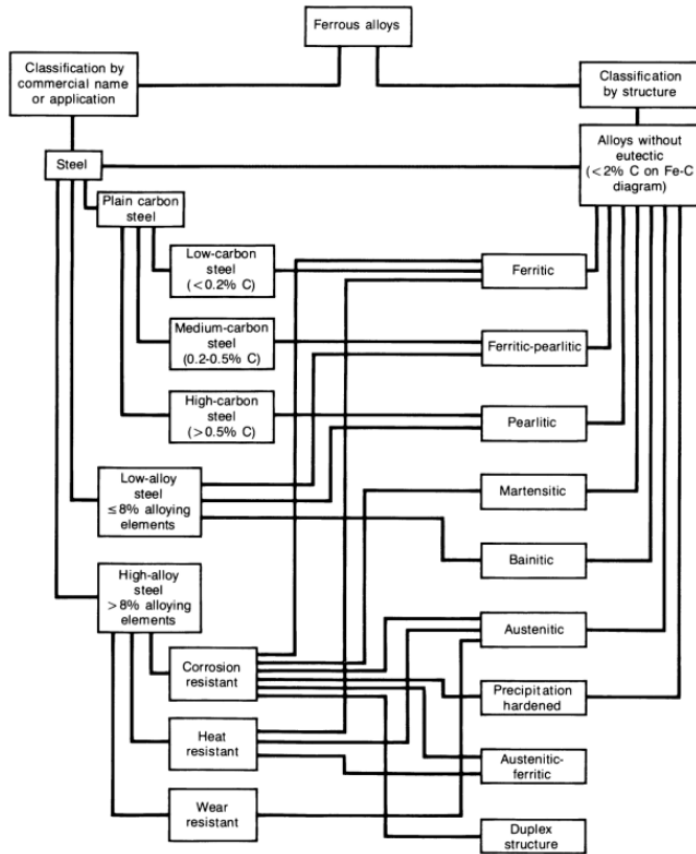


Figure 2.1 Classification of ferrous alloys[29].

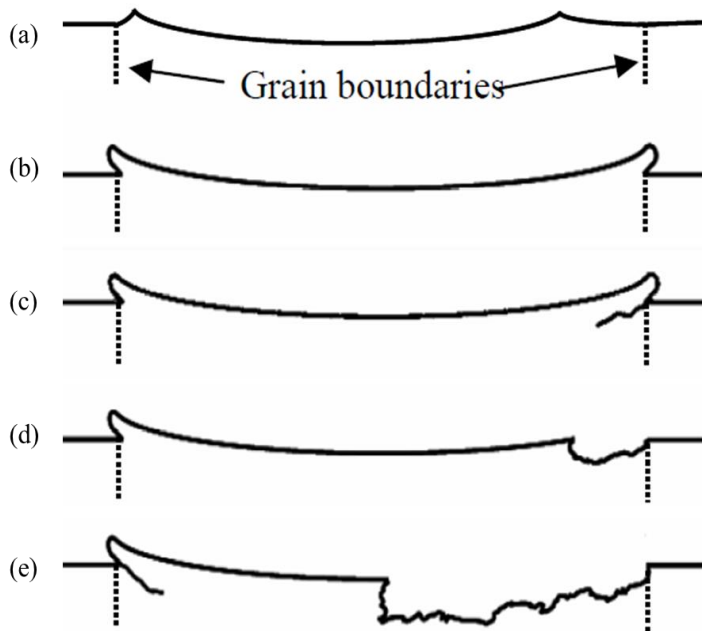
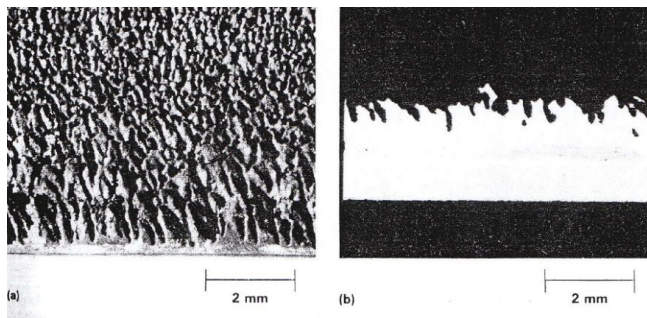
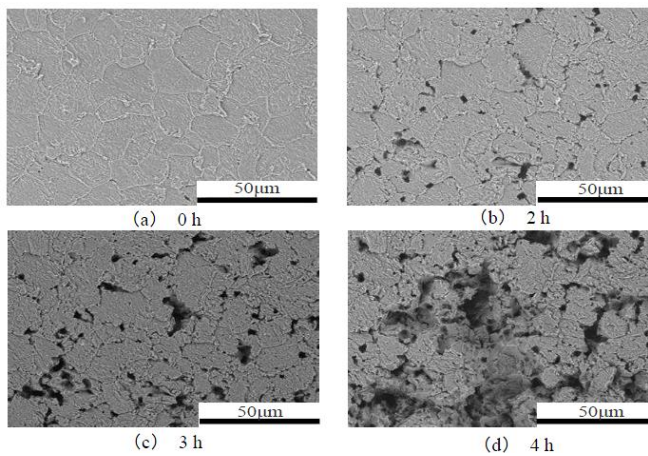


Figure 2.2 Schematic illustration of erosion damage process by liquid droplet impingement in ductile materials-(a) initial stage of erosion (b) plastic deformation at grain boundaries (c) crack initiation by fatigue (d) erosion on surface (e) further eroded surface[31].

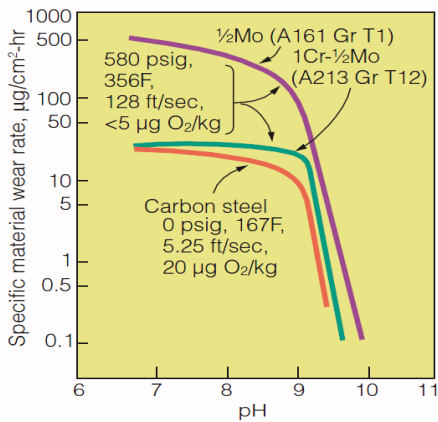


(a) Type 403 martensitic stainless steel

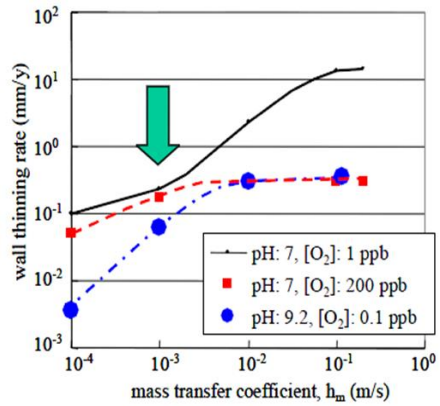


(b) S15C carbon steel

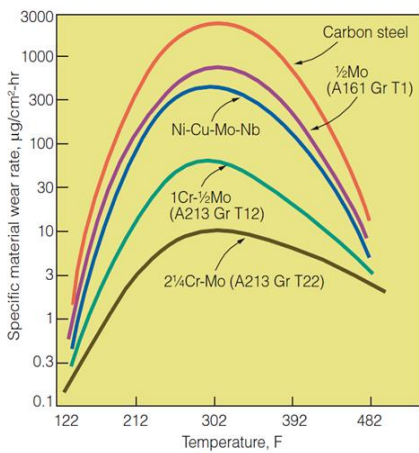
Figure 2.3 Microstructure of LDIE damaged specimen-(a) Type 403 martensitic stainless steel[28], (b) S15C carbon steel tested at 160 m/s of droplet velocity[31].



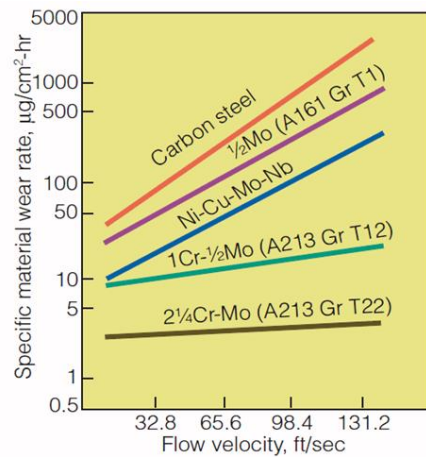
(a)



(b)



(c)



(d)

Figure 2.4 The environmental factor dependence on erosion-corrosion rate- (a) pH effect[41], (b) dissolved oxygen effect[39], (c) temperature effect[41], (d) flow velocity effect[41].

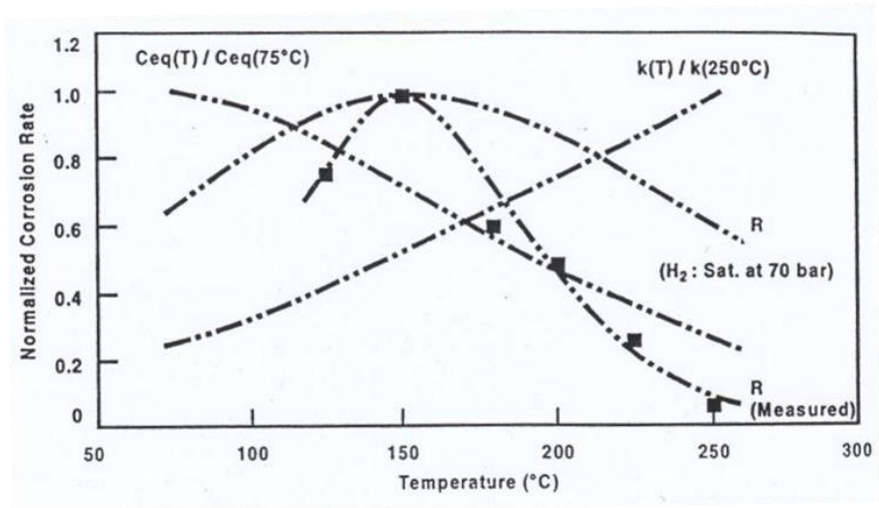


Figure 2.5 Temperature dependence of single-phase flow-accelerated corrosion with ammonia at pH 9.0(C_{eq} is magnetite solubility and k is mass transfer coefficient)[42].

2.3 Previous models for liquid droplet impingement erosion (LDIE)

When a physical phenomenon is fully understood, it should be possible to describe it mathematically in terms of a functional relationship between a set of dimensionless parameters. This ensures dimensional consistency in the functional relationships, makes the equations independent of the set of units of measurement adopted, and can help ensure that the correct number of independent parameters is included for each dependent parameter of interest. Unfortunately, no such complete relationship for predicting LDIE has been generally accepted to date, although some researchers have made attempt toward it.[44] However, systematic experimental work has been conducted in terms of each effective factor such as a droplet velocity, a droplet size, and so on.

2.3.1 Experimental models

Honegger[45] was the first investigator to notice the effect of exposure time on LDIE rate, Fyall[46], Adler[47], and Thiruvengadam[48] observed the influence of time on the instantaneous erosion rate. Investigations by Thiruvengadam and Preiser[35], Plesset and Devine[49], Heymann, Tichler and de Gee[50] have become classic studies. However, there have been several discrepancies in the agreement of the type of erosion rate versus time curves. Using the shapes of curves obtained earlier, many models and formulations have been presented by each investigator for the prediction of

LDIE. Each work was conducted at different number density of droplets and there is a variation on the droplet size distribution. Therefore, quantification of damage is not normalized to predict the damage in other environments.

Recently, an experimental model to predict LDIE has been developed by Isomoto[51,52]. The equation of thinning rate as follows,

$$T. R. = C_0 \cdot Hv^{-2.75} \cdot F_{freq} \cdot m_l \cdot V^2 \quad \text{Eq. (2.3)}$$

where C_0 is the coefficient, Hv is the Vickers hardness, GPa, F_{freq} is the collision frequency, $\text{mm}^{-2}\text{s}^{-1}$, m_l is the droplet weight, kg, and V is the droplet velocity, m/s.

An attempt to improve the Isomoto's model has been done and a new proposed model[53] adopting the cushioning effect which was proposed by Ikohagi[54,55], has been developed as follows,

$$T. R. = C_1 \cdot Hv^{-2.75} \cdot F_{freq} \cdot m_l \cdot V^2 \cdot (1 + C_2 \cdot t/d)^{-\alpha} \quad \text{Eq. (2.4)}$$

where C_1 , C_2 are the coefficients, t is the thickness of liquid film, mm, d is the droplet diameter, mm.

Both of the models depend on kinetic energy of droplets, collision frequency, and material hardness. In two-phase condition, though the cushioning effect has been obtained by an experimental correlation, it is hard to characterize the thickness of liquid film and subtle to generalize state quantities.

2.3.2 Corrosion-erosion combined models

Some research has been conducted on the combined action of the mechanical process of solid particle erosion and the electrochemical process of corrosion.[56] It is a common occurrence in the oil, gas, and mining industry as much as in chemical and power plants where it causes damage to the fluid handling components such as pumps, impellers, valves, and turbines. This may lead to the need of repair or replacement of these components which bring about high cost to these industries. To investigate the phenomena, the slurry pot erosion tester[57,58]has been used for the testing by changing the slurry medium to corrosive slurry.

However, the researches above focused on only solid particle erosion-corrosion which is not suitable to explain the corrosion effect on LDIE. There is a new approach to predict LDIE combined the corrosion effect[53,59, and 60].As aforementioned, the flow accelerated corrosion is widely known as a main mechanism of pipe wall thinning and ruptures in the secondary side of PWRs.

Koshizuka[59] evaluated a conceptual regime of the interaction of droplets with the secondary side pipe wall in terms of droplet velocities. The liquid droplet impingement divides into both corrosion and erosion dominant region according to droplet velocities. Naitoh[60] is developing a procedure to predict wall thinning rate by adopting three-dimensional computational dynamics (CFD) code combining a chemical reaction module.

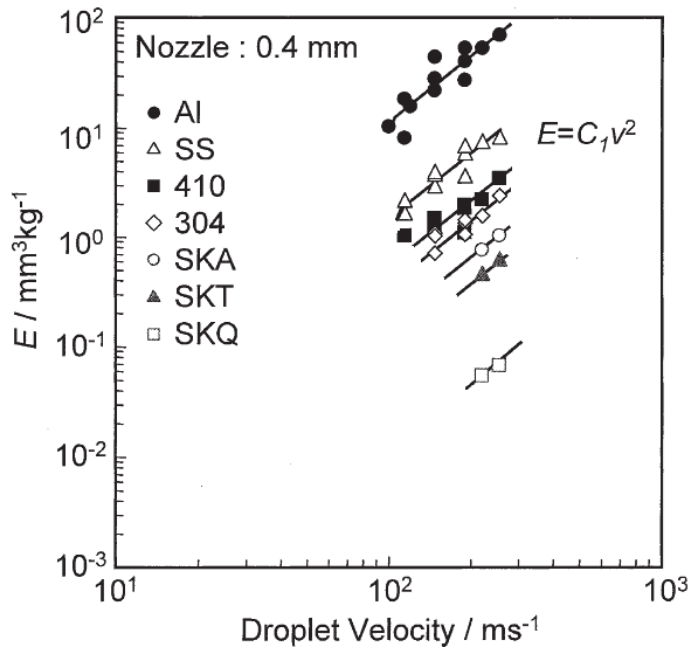


Figure 2.6 Wall thinning rate due to liquid droplet impingement[52].

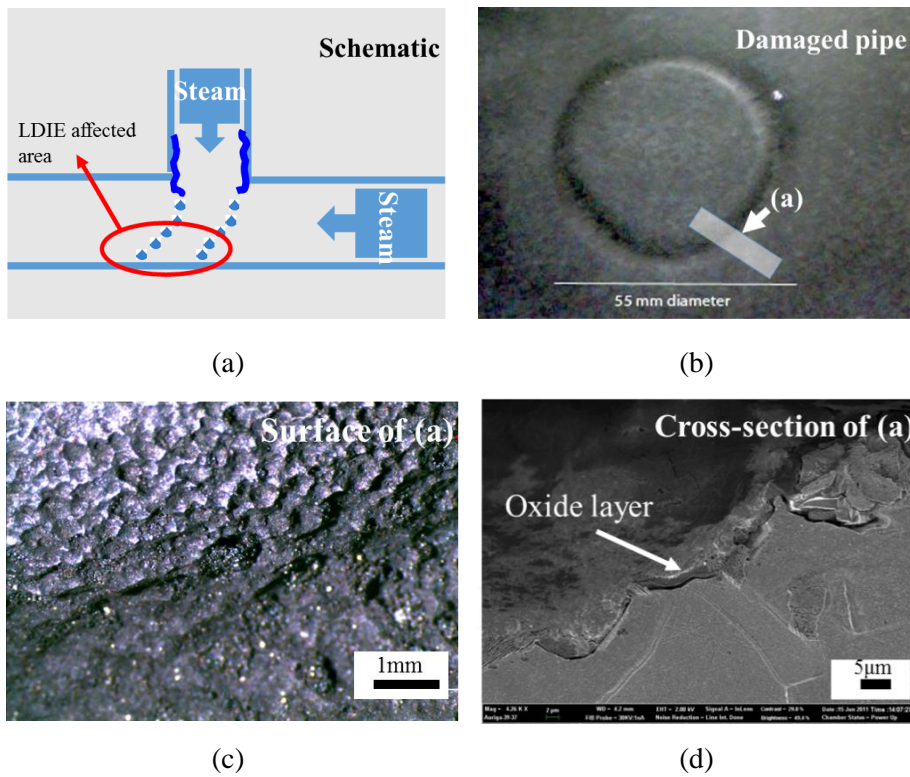


Figure 2.7 Field failure case-(a) schematic of damage scenario, (b) inner surface of damaged pipe, (c) microstructure of damaged surface, (d) cross-sectional image (A234 WPB, operated about 20 yr. at 138 °C)[4].

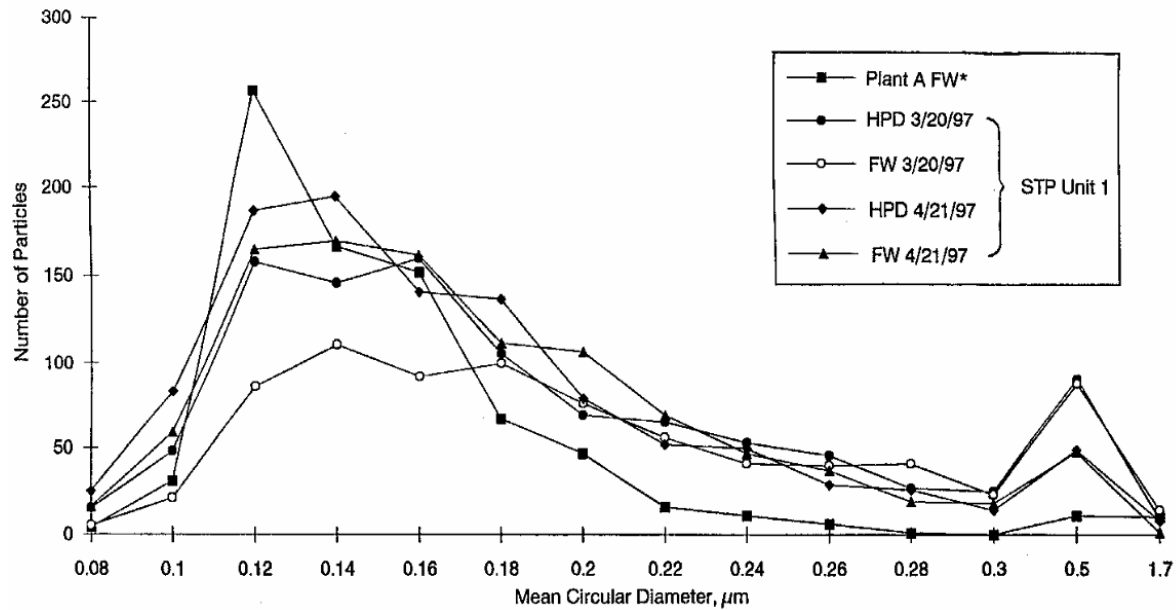


Figure 2.8 Corrosion product particle mean circular diameter distribution of high pressure drains and feedwater at South Texas Project Unit 1[61].

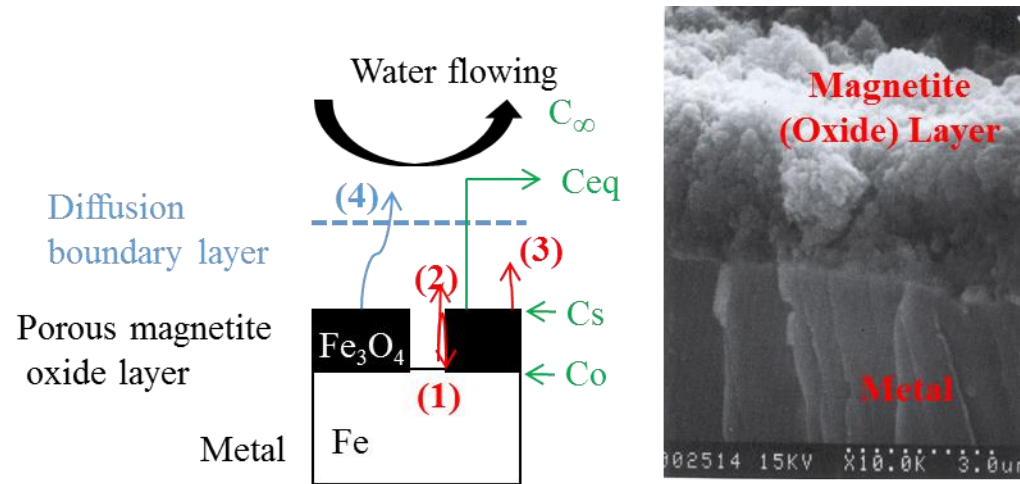


Figure 2.9 Flow accelerated corrosion model-(1) production of soluble ferrous ions at the iron/magnetite interface, (2) diffusion of soluble ferrous ions through porous oxide layer, (3) dissolution of magnetite at the oxide/water interface, (4) transfer of the ferrous ions into the bulk water across diffusion boundary[68].

Chapter 3. Rationale and Approach

3.1 Problem statement

Past research on the material degradation in the secondary side of PWRs has been focused on flow-accelerated corrosion (FAC). Although FAC is more frequent issue, LDIE has been identified recently as key causes of such pipe failures. Research on LDIE has been conducted on only in limited environment.

It is thus essential to the safety of plant crew that focused research efforts should be made on the damage mechanism, especially for the NPPs operating environment. Difficulties in conducting LDIE research arise from the fact that it take extraordinary approach (i) to simulate at the laboratory the LDIE phenomenon which arises in hosted environment over the span of several decades; and (ii) to identify the detailed mechanisms for such phenomenon due to the complex interaction among several effective factors.

3.2 Goals

The main objective of this thesis is to unravel the fundamental mechanism of LDIE. To achieve the goal, the specific tasks are defined as follows. Firstly a laboratory test apparatus which simulates the actual field conditions is to be developed. In order to achieve such acceleration of the pipe wall-thinning phenomenon, it is expected that the laboratory experiments should be conducted under appropriate water chemistry conditions. Both FAC and LDIE occur by water that contain lower content of ammonia compared with corresponding steam phase. Hence its pH is expected to be lowered and the corrosion is accelerated.

In the laboratory tests, two accelerating factors are employed; (i) the pH level is adjusted to a level lower than the pH level actually used in the secondary side of PWRs; and (ii) the velocity and size of water droplets are adjusted to levels higher than those actually existing at the secondary side of PWRs. In other words, it is intended to conduct this research by controlling the pH level, temperature, velocity and size of water droplets while keeping the dissolved oxygen (DO)/dissolved hydrogen (DH) concentrations and temperature at the same levels as those actually existing in the secondary side of PWRs. Keeping the redox conditions, the scene is important in maintaining the surface oxide layer composition and structure representation of actual field conditions.

3.3 Approach

The thesis investigation approach is summarized in Figure 3.1. To pursue the main objective of this research, understanding of LDIE mechanism, it is necessary to analyze test materials under high resolution microscopy with adequate material selection. The analysis of the experimentally by produced damage are conducted by micro and nano-structural analysis as well as quantitative assessments. Mechanistic understanding from microscopic analysis can be confirmed by the relationship between effective factors and damage rates. A semi-empirical model on the damage rate can be developed based on damage mechanism. The model will be verified by field data using actual operation conditions.

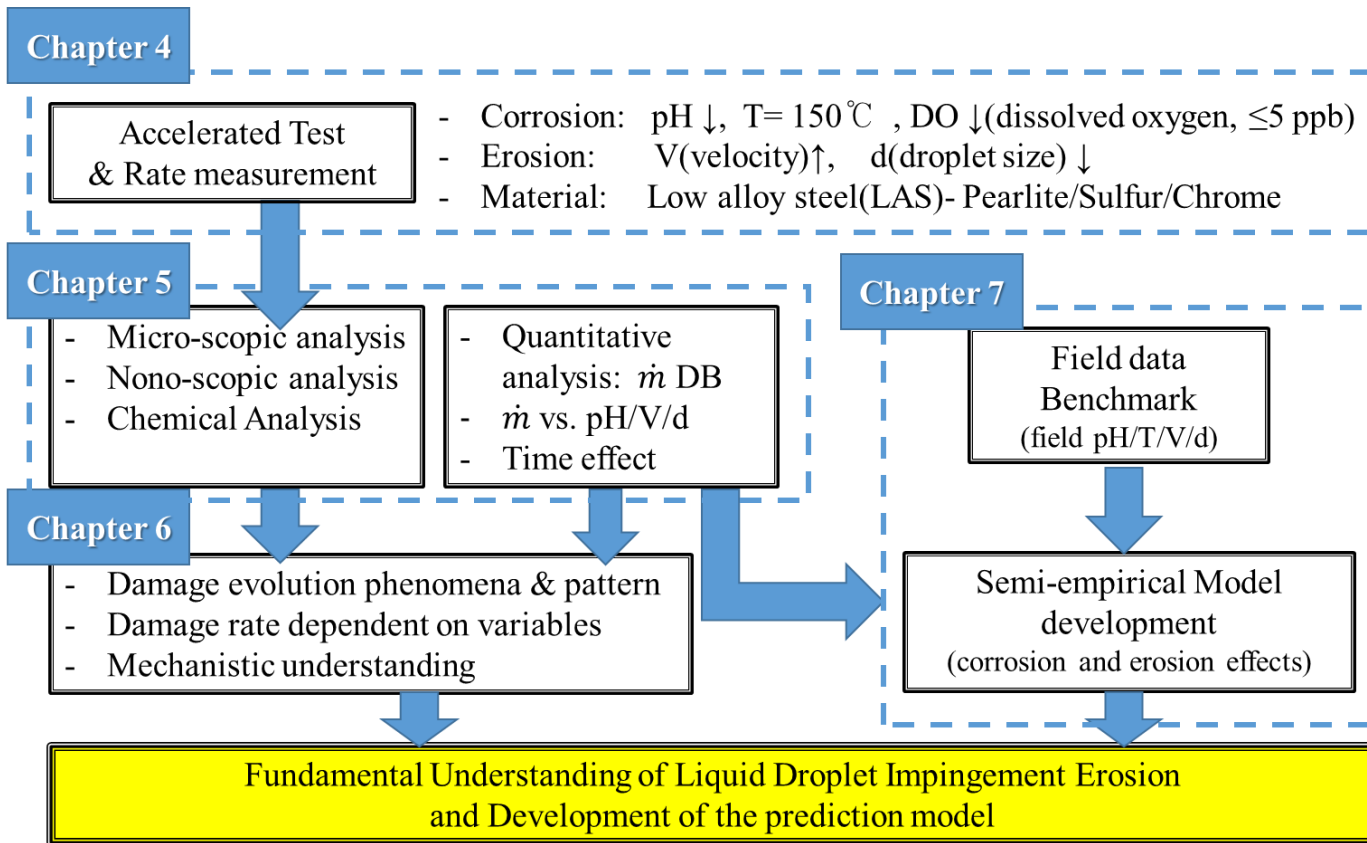


Figure 3.1 Diagram for LDIE mechanistic study

Chapter 4. Experimental Design and Procedure

4.1 Microstructure and chemistry of materials

As test material representing purpose, ASTM A106 Gr. B (UNS K03006) was chosen because it has been widely used in the secondary side of PWRs.[4] alternatives material including A335 P22 (UNS K21590), and SUM24L (UNS G12144) were chosen to investigate composition effects on the LDIE damage. The chemical composition and yield strength are summarized in Table 4.1. A 106 Gr.B and A335 P22 were manufactured by JFE Steel Corp. and Sumitomo Metal Industries Ltd., Japan, respectively. In as-received conditions, A106 Gr.B. was hot-finished at 780°C and fully killed, i.e. perfectly de-oxidized. A 335 P22 was heat-treated by isothermal annealing treatment at 720°C for 45 minutes.

Carbon is essential to the strengthening of steels and the formation of cementite (Fe_3C), and hence to the formation of pearlite. Mn slightly increases the strength of ferrite, and also increases the ductility and toughness of steel.

It was known that Cr is a key alloying element for corrosion resistance at high temperature applications. Increased Cr content improves oxidation and corrosion resistance. Cr can also increase the toughness of steel, as well as the wear resistance.[61] Si is used as a de-oxidizer in the manufacture of steels. It can improve weldability and can slightly increases the toughness of ferrite,

and when used in conjunction with other alloys can help increase the toughness and hardness penetration of steel.[61] Ni increases the strength of ferrite, therefore increasing the strength of the steel. It is used in low-alloy steels to increase toughness and hardenability.

Usually, the hardness of steels is linearly proportional to its yield strength[61]. The test materials have a range of yield strength hence it is expected that the damage rate due to LDIE may vary accordingly.

The optical microstructures of all tested materials are shown in Figure 4.1. The metallographic specimens were prepared by wire electrical discharge machining (EDM) to its size, 14 mm (width) x 30mm (length) x 3 mm (thickness). The surface has been polished up to 0.1 μm Al_2O_3 suspension. The 2% nital etching and drying showed the pearlite and ferrite structures as shown in Figure 4.1. Both A106 Gr.B and A335 P22 exhibit similar prior austenite grain size. Their pearlite subgrains have about 30 μm diameter. Particularly, the SUM 24L shows banded pearlite structures along the rolling direction (R.D.) as shown in Figure 4.1 (c).

Optical microscopic results have limited resolution and it is too difficult to analyze the details of microstructures. Therefore, nanostructure analysis has been made by using the field emission scanning electron microscopy (FE-SEM, model name SIGMA, Carl Zeiss, 1.0 nm resolution at 15 kV). Results are shown in Figure 4.2. The pearlite structure is well characterized by a lamellar morphology composed of alternating layers of alpha-ferrite and cementite. In photomicrograph of Figure 4.1, the pearlite regions can be identified as dark areas in the nital-etched specimens. The spacing among

cementite layers is a few hundreds of nanometer, and one cementite layer has a thickness that is several tens of nanometer.

Table 4.1 Chemical composition and yield strength of LDIE test materials(wt.%)

	C	Si	Mn	P	S	Cu	Pb	Ni	Cr	Mo	σ_y (MPa)
A106 Gr.B (UNS K03006)	0.28	0.1	1.16	0.03	0.03	0.04	-	0.40	0.40	0.15	288
A335 P22 (UNS K21590)	0.15	0.5	0.6	0.025	0.025	-	-	-	2.6	1.13	210
SUM24L (UNS G12144)	0.068	-	1.088	0.05	0.316	-	0.27	-	-	-	415

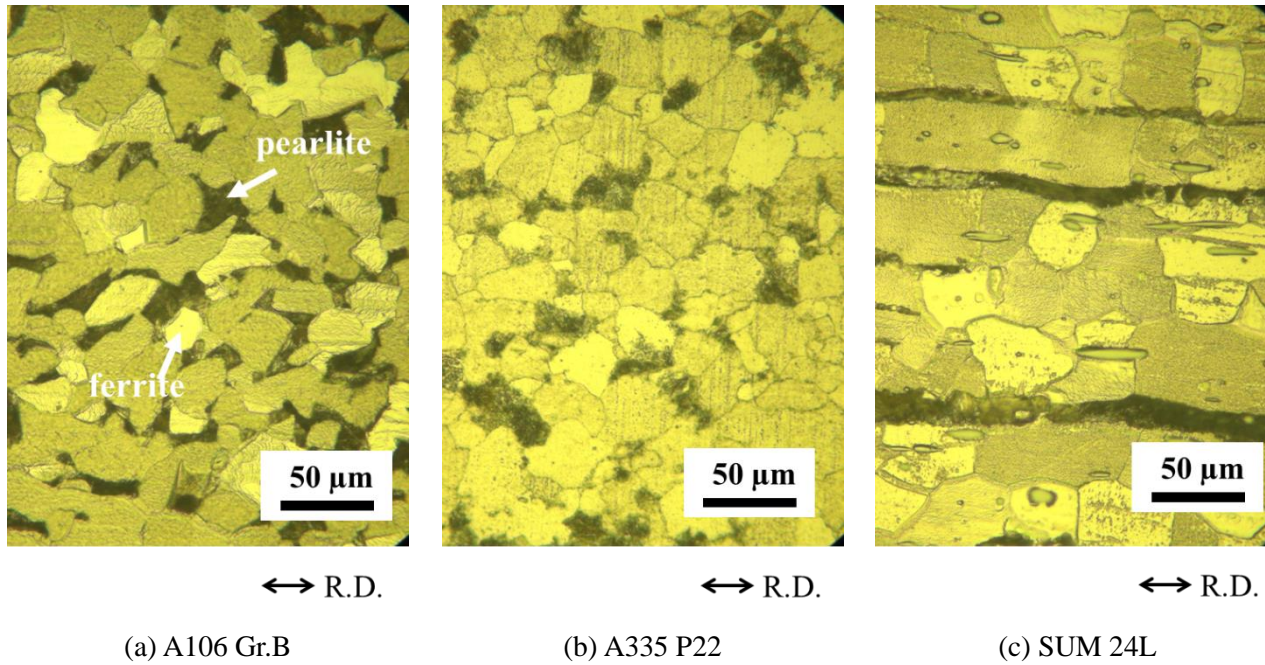
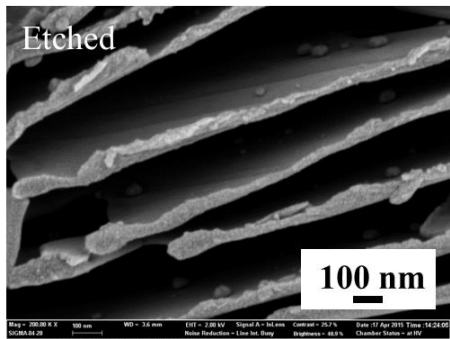
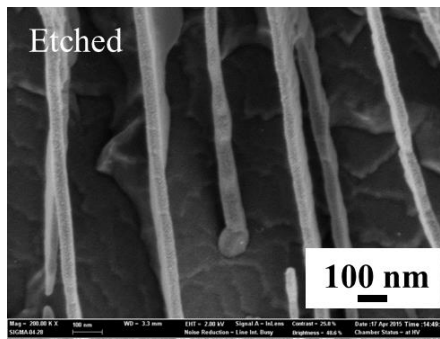


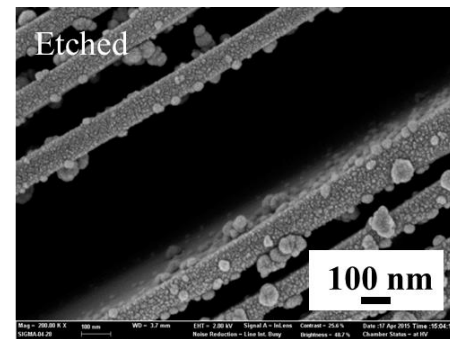
Figure 4.1 Photomicrographs of 2% nital etched test materials; (a) A106 Gr.B, (b) A334 P22, and (c) SUM24L.



(a) A106 Gr.B



(b) A335 P22



(c) SUM24L

Figure 4.2 Nanoscale photomicrographs of test materials revealing cementite layers left as a result of dissolution of ferrite layers in between (FE-SEM).

4.2 Development of the LDIE accelerated test apparatus

To accelerate the LDIE damage in laboratory experiments, the test apparatus has been developed to include two systems. The first is a chemical balancing system which can control the water chemistry where the pH level of chemical water is adjusted to a level lower than the pH, dissolved oxygen (DO)/dissolved hydrogen (DH) concentrations, and temperature are also regulated to the same conditions as the secondary side of PWRs. An impingement test system is consisted of the rotating machine. The conceptual design of the impingement test system was based on ASTM standard method, named ASTM method G73-10[62].

There are three types of ASTM standard methods for liquid droplet impingement test, including high-frequency vibratory method, water-jet method, and rotating machine method[62-64]. The vibratory method is suitable for bubble-induced erosion which has no relevance to the LDIE. Secondly, water-jet method is recommended as a proper method that can easily simulate the LDIE damage, but the control of droplet size and distribution is complex due to very high pressure and velocity of droplets. Finally, the rotating machine method is chosen because there are clear advantages in controlling droplet speed and size. The droplet velocity can be controlled by rotor speed and droplet size can be controlled by liquid nozzle size and stand-off distance (SOD)[65].

Therefore, the developed apparatus in this thesis followed ASTM method G73-10 as delineated in Figure 4.3. The rotating disc is composed of a spinning arm and a circular rotating disc. The energy required to rotate the

disc can be calculated by the Equation 4.1-2 as follows[66],

- (i) The energy consumption by a disc, P_D

$$P_D = C_m \frac{\rho_a}{2} \omega^3 R_D^5 \quad \text{Eq. (4.1)}$$

where

C_m : moment coefficient

ρ_a : density of air, kg/m³

ω : angular velocity of air, s⁻¹

R_D : radius of disk, m

- (ii) The energy consumption by a circular rotating disc

$$P_a = C_D \rho_a \omega^3 c \left(\frac{R_0^4}{4} - \frac{R_i^4}{4} \right) \quad \text{Eq. (4.2)}$$

where

C_D : drag coefficient of the aero foil

C : chord length of aero foil, m

R_0 : outer radius of the disc, m

R_i : inner radius of the disc, m.

Since the energy consumption by installed specimens is less than those by the circular rotating disc and the spinning arm, the energy consumption by installed specimens was ignored. A rotating disk does not require a high torque because it does not often accelerate or decelerate the speed. From the

calculated results, a 3600 RPM-2P-10HP Motor has been equipped with a sufficient margin.

The LDIE test chamber was designed according to ASME Sec. VIII Div.1[67]. From the rule of “UG-27 thickness of shell under internal pressure” in the Div.1, the minimum thickness of the vessel was chosen as a higher value in the result from the stress calculation between circumferential and longitudinal stress. The maximum allowable stress of the test chamber was referenced in Type304 stainless steel and the required thickness was calculated by Equations (4.3) and (4.4) as follows.

- (i) The required thickness by circumferential stress

$$t = \frac{PR}{SE - 0.6P} \quad \text{Eq. (4.3)}$$

- (ii) The required thickness by longitudinal stress

$$t = \frac{PR}{2SE - 0.4P} \quad \text{Eq. (4.4)}$$

where

t: minimum required thickness of vessel, m

P: internal design pressure, kPa

R: inside radius of vessel, m

S: maximum allowable stress, kPa

E: joint efficiency, 0.85.

The thickness of flat head in both side of vessel can be defined by “UG-34 un-stayed flat heads and covers” in the Div.1 of ASME Sec. VIII. In bolt or flange union cases, the required thickness t was derived in Equation (4.5) as follows. The standard on flange specification and required bolt cross-sectional area defined by applied force to the bolts is described in Appendix 2 2-5 in the Div.1,

$$t = d \sqrt{\frac{CP}{SE} + 1.9 \frac{Wh_G}{SEd^3}} \quad \text{Eq. (4.5)}$$

where

C: a factor depending on attachment method, 0.3

P: internal design pressure, kPa

D: diameter, m

S: maximum allowable stress, kPa

E: joint efficiency, 0.85

W: total bolt load, kg

h_G : gasket moment arm, m.

Figure 4.4 shows the piping and instrument diagram (P&ID) for the LDIE simulation test system. The water passes through pH meter and then to a charging pump that pumps water into a test loop. Because iron dissolution process changes pH, a continuous monitoring and controlling of pH is maintained. Monitored pH of auto pH control system put nitric acid into the

chemical water tank that maintains the water chemistry. The chemical water in the tank is bubbled by 4% hydrogen gas, which makes nitric acid mixed with chemical water and removes dissolved oxygen in the water. The charging rate to the test loop is 720cc/min that is sufficient to fill the loss of a nozzle installed to impinge specimens. Chemical water is pressurized to 12 atm and is circulated by a circulation pump. Various parameters such as dissolved oxygen, dissolved hydrogen, temperature, and pH are continuously monitored and maintained at the designed test condition.

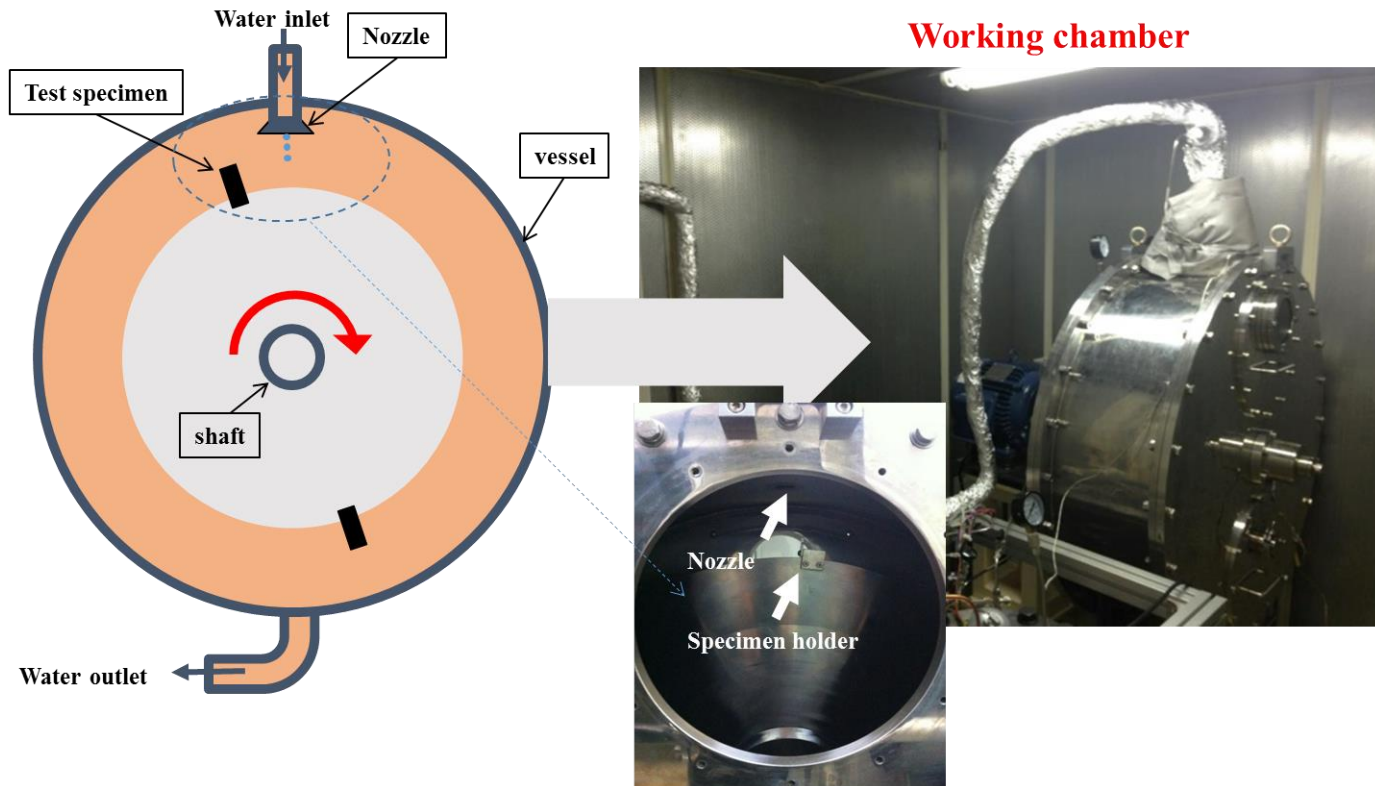


Figure 4.3 The schematic of LDIE test apparatus based on ASTM G73-10 standard method

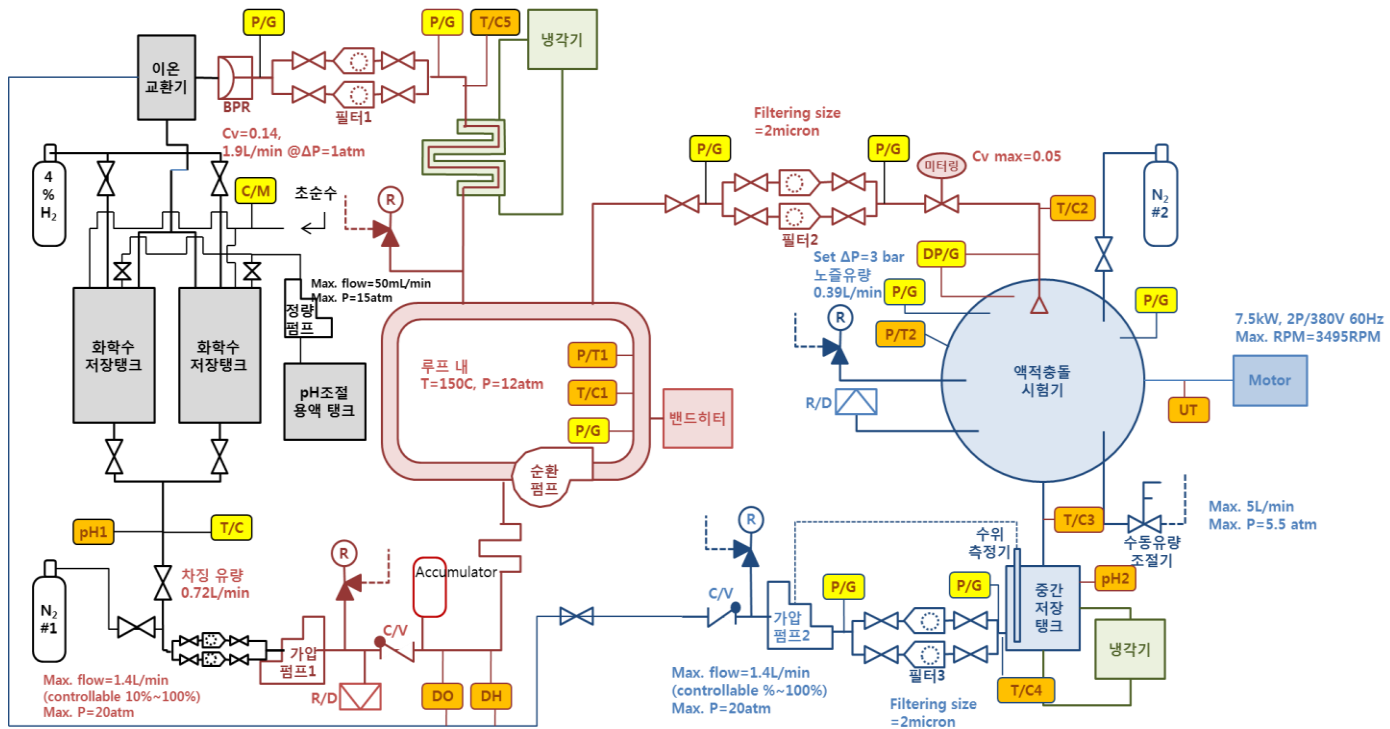
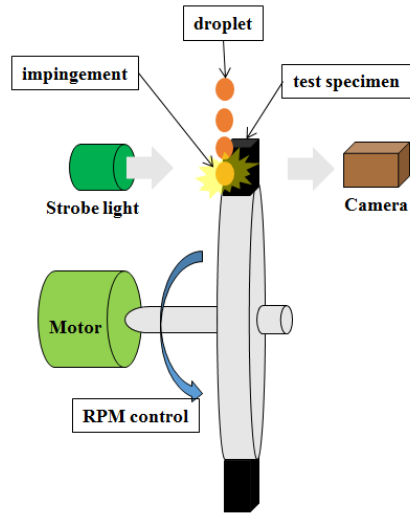
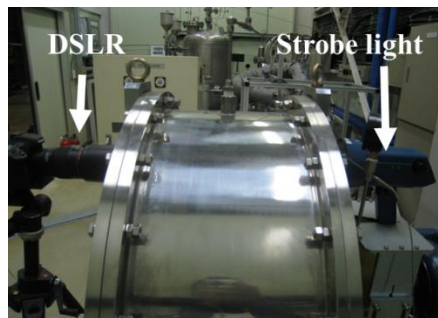


Figure 4.4 Piping and instrument diagram (P&ID) for balancing water chemistry and recirculation

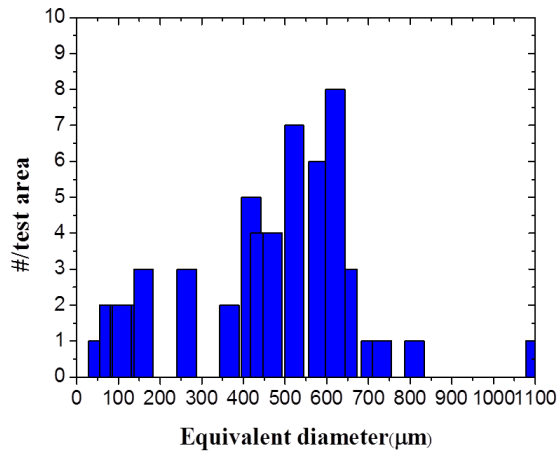


(a)

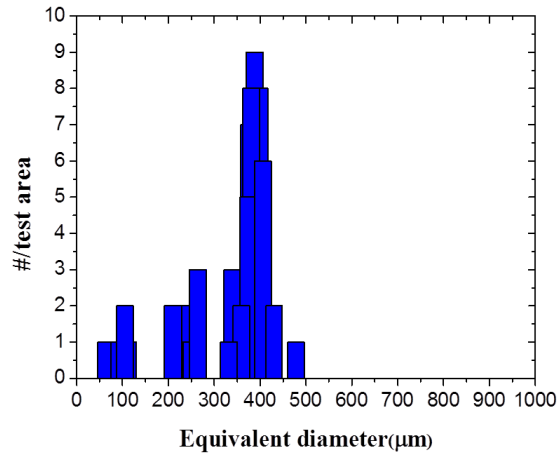


(b)

Figure 4.5 Droplet characteristics measurement-(a) schematic of droplet size measurement, (b) droplet size measurement system by using DSLR and strobe light



(a) SMD- 613 μ m (Nozzle size, 600 μ m)



(b) SMD-379 μ m (Nozzle size, 400 μ m)

Figure 4.6 Droplet diameter and distribution-(a) Sauter mean diameter(SMD) is 613 μ m for Nozzle size(600 μ m), (b) Sauter mean diameter(SMD) is 379 μ m for Nozzle size(600 μ m).

4.3 Test matrix and test procedures

LDIE experiments have been conducted for those test materials under the test conditions as shown in Table 4.2 together with measurement error which is allowed in the instrument and equipment control. The test matrix was designed systematically to investigate the effect of key factors on the LDIE damage rate.

As aforementioned, the corrosion of LAS in flowing water is dependent on flow velocity and temperature. The maximum corrosion can be expected to occur at 150°C for LAS in the secondary water of PWRs[42]. Therefore, the temperature of the LDIE experiments was fixed at 150°C.

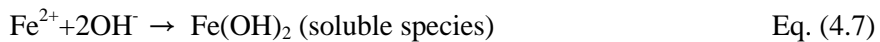
In addition, during the plant operation, the structure of iron oxide film formed on the LAS surface controlling corrosion rate. It is reducing environment of the secondary side of PWRs in which the oxygen concentration is less than 5 ppb, the iron oxide form as magnetite with hydrazine injection. To accelerate the LDIE damage and investigate the corrosion mechanism in the field operating conditions, the test condition should maintain the same electrochemical condition of the secondary side of PWRs. Figure 4.7 shows a Pourbaix diagram which represents relationship between electrochemical equilibrium potential and pH. The region marked by a black box represents identical electrochemical condition for oxide film structure; magnetite. Therefore an accelerated test condition in these experiments shows the magnetite region is determined by lowering pH in the black box. The dissolved oxygen level was maintained at lower than 5 ppb in all experiments.

The pH level at 25°C was lowered to 4 to 6 below actual value of pH (~9.2) in the secondary side of PWRs. The magnetite solubility increases as pH decreases so that the corrosion effect can be accelerated in the same electrochemical condition and oxide structure. The LDIE phenomena between metal and water interface has been simulated as a function of pH in reducing environment at 150°C.

Magnetite is porous and water can penetrate through so that direct reaction with substrate iron can be modeled[68]. The iron oxidation occurs at the iron-magnetite interface in reducing condition by following reactions;



As the result, the pH of water increases as Fe^{2+} concentration increases. Both ferrous ions and iron hydroxides can be obtained at high pH according to an equilibrium reaction;



The second process of the iron hydroxide reaction with water leads to magnetite (Fe_3O_4), through the Schikorr reaction;



Dissolved ferrous ions diffuse from the iron surface to the water through magnetite which has a porous structure. The magnetite oxide layer at the oxide-water interface can also dissolve by a reductive process by the presence of hydrogen. The hydrogen comes from the injected hydrazine;



Magnetite formation in reducing water was precisely described by Sweeton and Baes[69]. From the Sweeton and Baes's result, the magnetite solubility, C_e at equilibrium, can be calculated in Figure 4.8. The magnetite solubility is dependent on temperature as well as pH.

All of LDIE test specimens were prepared by wire cut electrical discharge machining (EDM) and its size is 14 mm (width) x 30mm (length) x 3 mm (thickness). A rectangular area, 14 x 30 mm², was exposed to water droplets as demonstrated in Figure 4.3. The surface of specimens has been with SiC paper with water as lubricant from 320 to 1200 grits, and then diamond suspension with 6 to 0.1 μ m size was used to polish that surfaces.

The actual damaged area is one-half of a specimen area because the area except the test area was blocked by a fixture of teflon plate in the LDIE test disc. To measure the mass loss, a SHIMADZU model AUW220D electronic scale was used. The electronic scale was calibrated to have a $\pm 10^{-5}$ g of linearity error (82g range)[70]. To shorten exposed time into the air and remove humidity on the specimen surface, ethanol rinsing was adopted after taking out from the chamber.

Table 4.2 LDIE test matrix and the error of measurement (at 150 °C, less than 5 ppb of dissolved oxygen)

Factor(unit)	pH	V(m/s)	d(μ m)
Test #	± 0.1 (error)	$\pm 5\%$ (error)	$\pm 40\mu$ m(error)
#1	4	120	600
#2	4	80	600
#3	5	80	600
#4	5	120	600
#5	4.5	80	600
#6	4.5	120	600
#7	4	100	600
#8	4	80	400
#9	4	100	400
#10	4	120	400

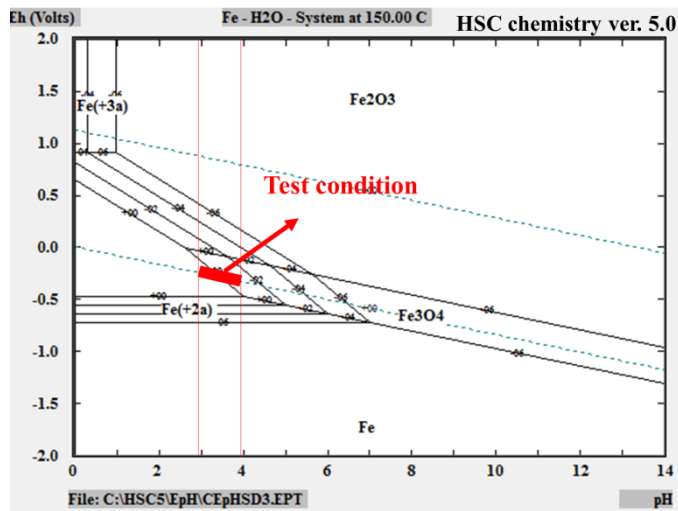


Figure 4.7 pH and electrochemical potential under test conditions calculated by HSC chemistry[70].

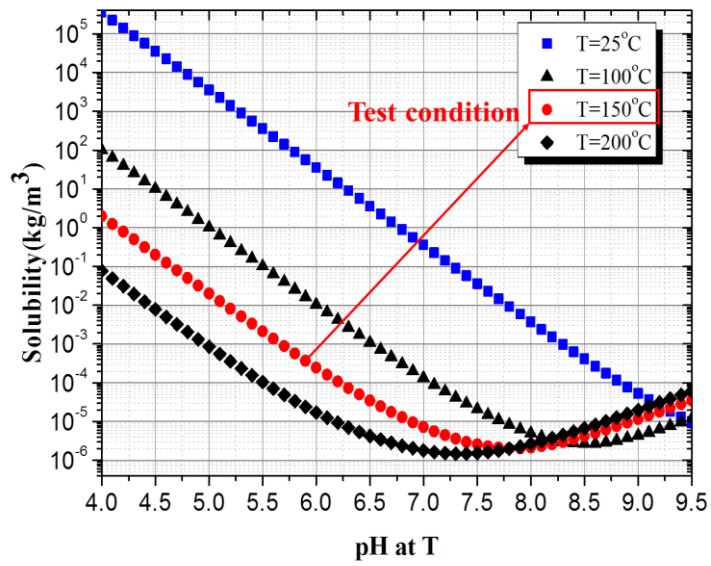


Figure 4.8 Magnetite solubility as functions of temperature and pH[69].

Chapter 5. Experimental Results

5.1 Analysis of experimental results

Experimentals have been conducted at 3, 2, and 3 levels of droplet velocity, droplet size, and pH respectively for the three types of materials. In the first series of test, the test duration was kept at 96 hours in each test condition. Four specimens were tested simultaneously for each material. The mass loss was measured by removing specimens at the end of each 24 hours following the above procedures. During the damage test period, the inlet water temperature was maintained at $150^{\circ}\text{C} \pm 2^{\circ}\text{C}$, as measured by a Type K thermocouple located in the tube before entering the nozzle. The dissolved oxygen (DO) is also maintained at less than 3.2 ppb. After test was completed, the impinged surface of all test specimens was covered with black-colored oxide layer. When analyzed by X-ray diffraction (XPS) method, the surface layer has been identified as magnetite (Fe_3O_4).

Figure 5.1 shows the relationship between the pH and the mass loss of specimens at the same droplet velocity (120m/s) and droplet diameter ($600\ \mu\text{m}$) condition. For all materials, as pH increases, the mass loss rate drastically decreases. As a result, in the mass loss at pH 5 condition, total mass loss during 96 hours did not exceed 10 mg.

At the lowest pH condition (pH 4 at 25°C), it shows an interesting feature that there is a rate change during the tested time. Interesting material dependence is displayed by A106 Gr.B and A335 P22. As time increases, the

mass loss rate increases for both materials. However, the case of A335 P22 showed that the mass loss rate remains lower than that of A 106 Gr. B before a transition time. After the transition point, the mass loss rate of A335 P22 rapidly increased above the rate of A 106 Gr. B.

Figure 5.2 shows the relationship as function of droplet velocity and the mass loss of specimens at pH 4 and droplet size of $600\ \mu\text{m}$. As the droplet velocity increases, the mass loss rate also increases in both materials. In early period, the mass loss rate of A335 P22 is lower than that of A 106 Gr.B. After transition point the rates of two materials were reversed. From the results, it is found that there is a transition point at a specific time where the mass loss rate changes to higher orders.

Figure 5.3 shows that the relationship between droplet diameter and the mass loss of specimens at the same droplet velocity (120 m/s) and pH (pH 4). The results show that the LDIE damage is obviously dependent on the droplet diameter. In both cases of 400 and $600\ \mu\text{m}$ of droplet diameter, the results show identical transition at around 48 hours. After the time, the mass loss rate transition occurred in both cases.

To investigate the long-term behavior after the transition, the impingement test was conducted for up to 200 hours. Figure 5.4 shows the mass loss of test materials including SUM24L as a verifying an alloying effect as time increase. The test was conducted at a constant of droplet velocity and size with a low pH (pH 4) condition. The objective of the long-term test is to identify any other transition behaviors. After 150 hours, the mass loss rates of test materials are stabilized to constant values. The reverse of mass loss rates

between A106 Gr. B and A335 P22 is not shown in previous results because the number density of impinged droplets is not same.

5.2 Microstructural evolution of damages

From the experimental results, it has been found that the LDIE rate is dependent on each parameter. The mass loss increases as pH decreases drastically. It means that the damage rate can be affected by pH effect, although the LDIE is an erosion process. As aforementioned, the iron solubility increase as the pH decreases. It leads to accelerate the dissolution of iron ions and the oxidation of iron oxide and its dissolution.

Before advanced analysis for nano-structures, the optical analysis was conducted on the damaged specimens. Figure 5.5 shows the microstructure of damaged A106 Gr.B specimen as the test time increases at the same area. As shown Figure 5.5(a), the initiation of damage is localized in specific areas. Figure 5.5(b)-(c) shows the damage deepen into the depth of grains at the same area of Figure 5.5(a). Figure 5.5(d) shows significantly damaged area and dark area in which the oxide layers formed.

Before the test, the microstructure of a field specimen was investigated as shown in Figure 5.6. The damaged material is A234 WPB which is a carbon steel and the chemical composition is quite same with A106 Gr.B. The cross-sectional area shows stringers of sulfide (Figure 5.6(a)) and carbon rich phase (Figure 5.6(b))

From the microstructure, hypothesis can be made that (i) MnS initiates the damage, (ii) selective dissolution of iron in pearlite grains. To verify the

hypothesis (i), mechanism verification test was conducted as shown in Figure 5.7. The sulfur content of SUM24L is about ten times higher than A106 Gr.B or A335 P22. The existence of sulfide in both materials was confirmed according to sulfur printing of A106Gr.B(Figure 5.8(a)) and electron diffraction spectroscopy (EDS) of SUM24L(Figure 5.8(b)). However, in the initiation of the LDIE test, the mass loss rate of SUM24L is similar with the rate of A106 Gr.B. From the results, it is judged that the MnS is not the root cause of the initiation of the LDIE. From the damaged specimen of A106Gr.B, it is postulated that the damaged area correspond with the pearlite grains. To investigate the postulate, more detailed micro and nano-structure analysis have been made and the details of the result will be discussed separately in Chapter 6.

It is noticed that there is transition period in which the LDIE rate is changed. To find the damage mechanism, it is important to understand the meaning of the transition phenomena which can be governed by different dominant mechanisms.

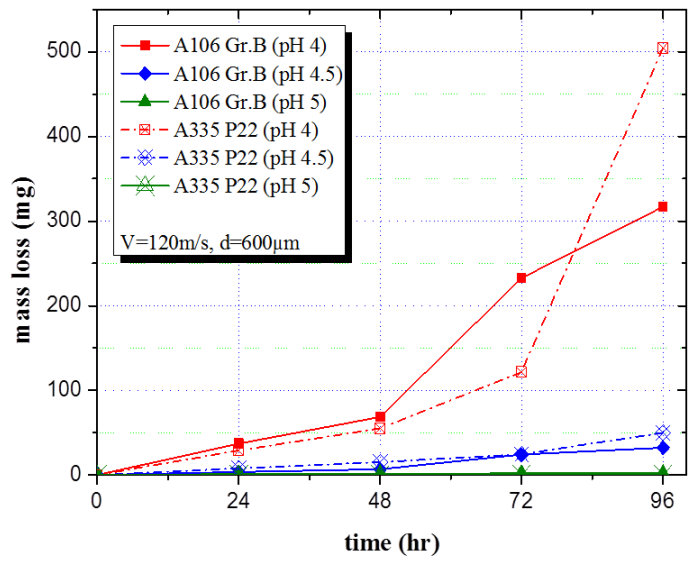


Figure 5.1 Mass loss of LAS as a function of pH.

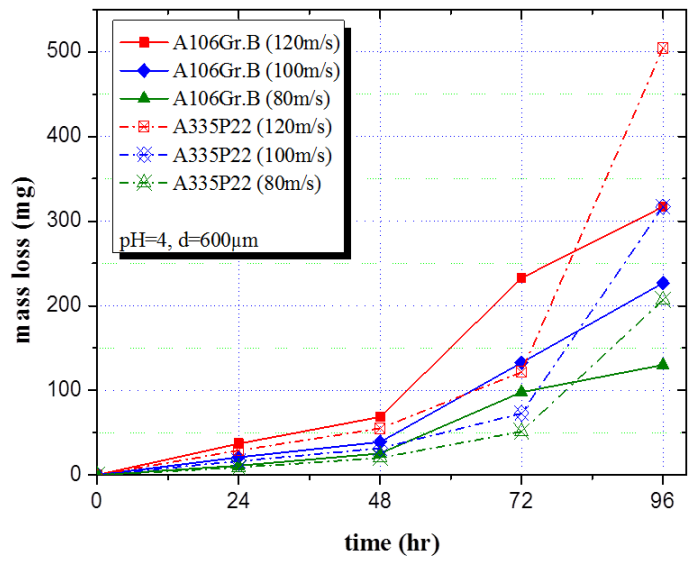


Figure 5.2 Mass loss of LAS as a function of droplet velocity.

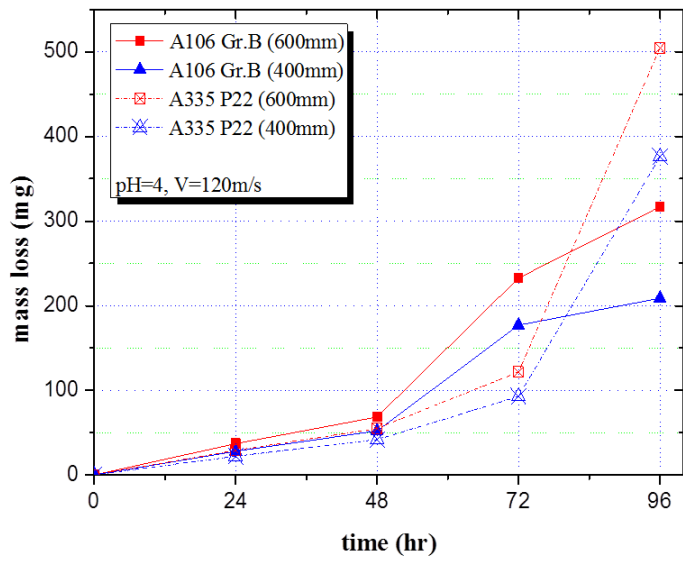


Figure 5.3 Mass loss of LAS as a function of droplet diameter.

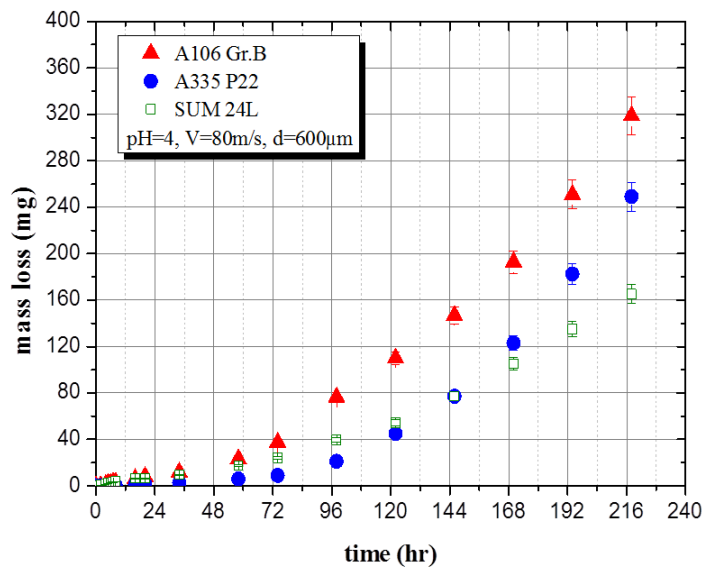


Figure 5.4 Long-term experiment for up to 200 hr.

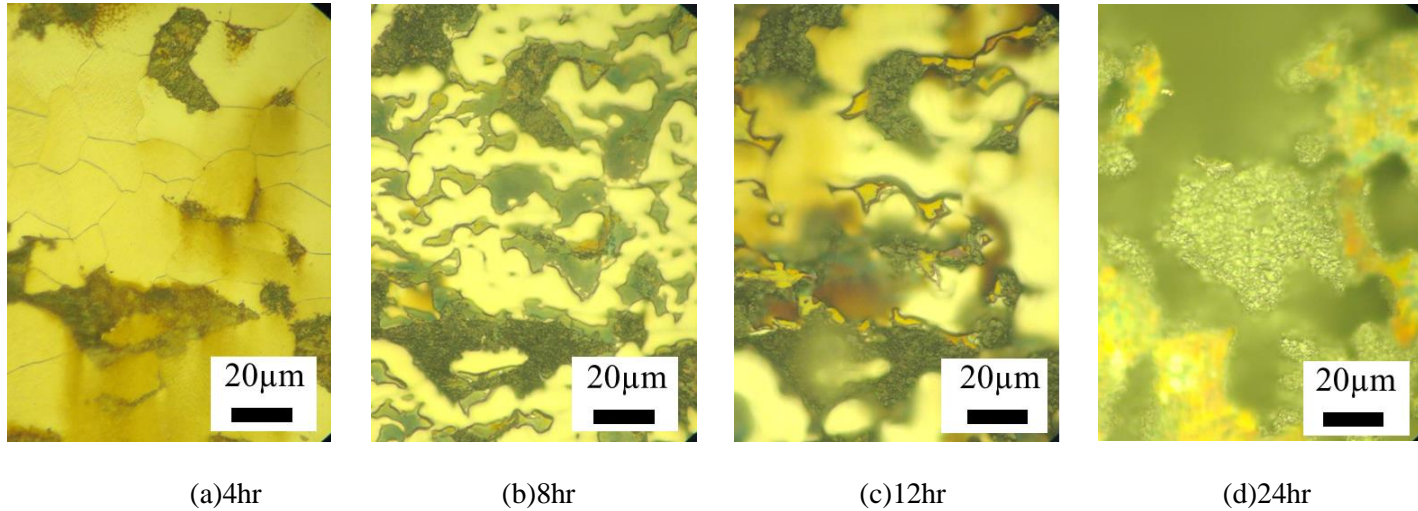
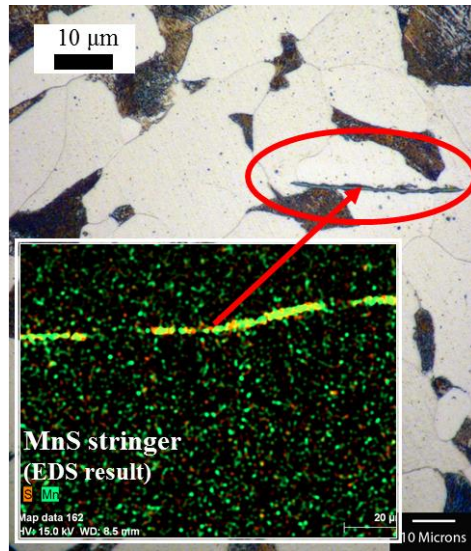
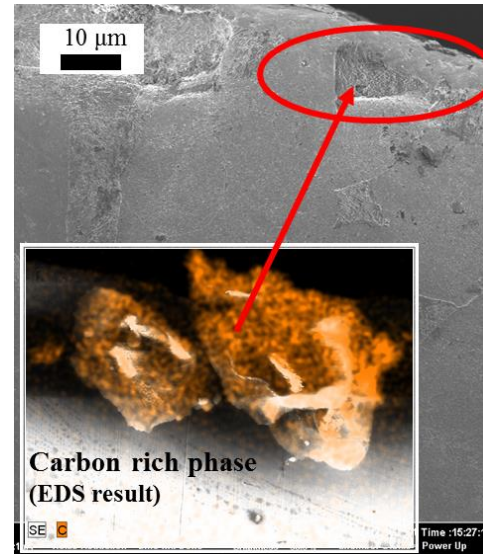


Figure 5.5 Time dependence of microstructures of A106 Gr.B (pH-4, V-80m/s, d-700µm, T-150°C, x1000 magnification)



(a)



(b)

Figure 5.6 Cross-sectional microstructure of a field failure specimen –(a) MnS stringer in both optical microscope and EDS), (b) Carbon rich phase near damaged surface

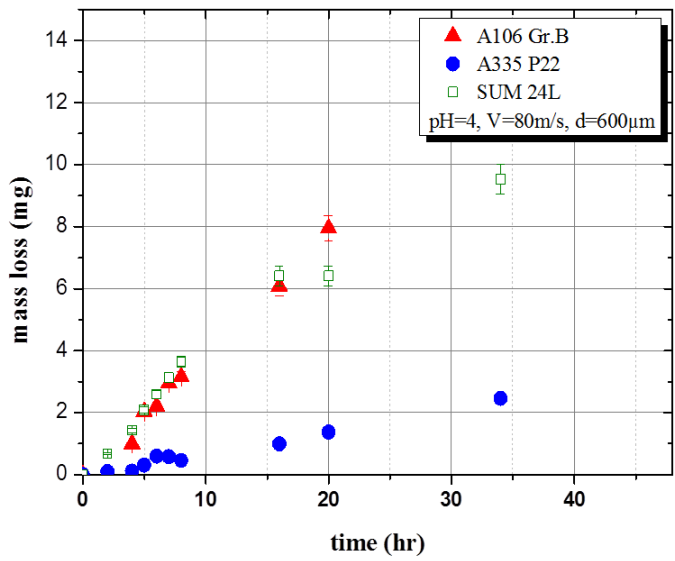
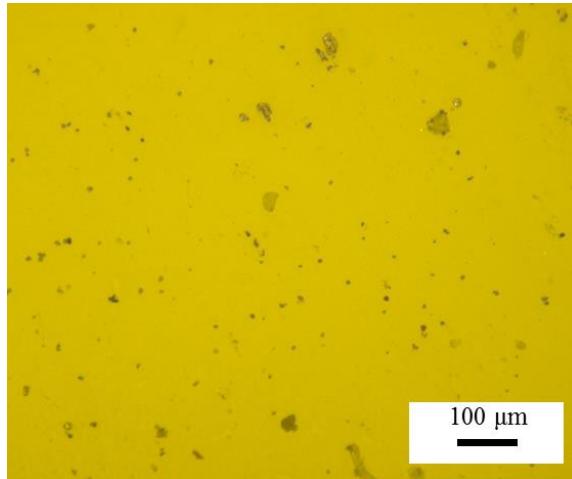
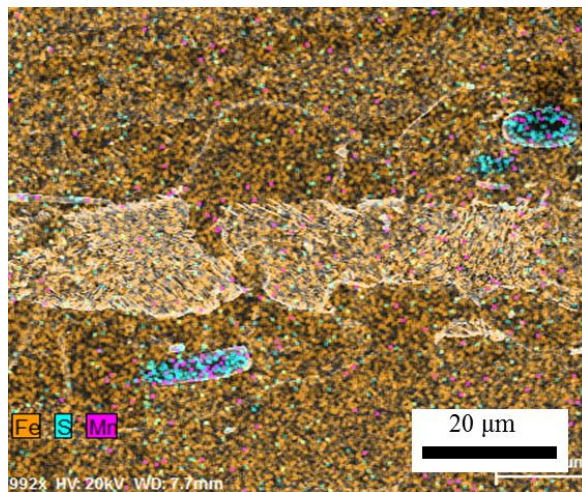


Figure 5.7 Initiation stage of LDIE damage-dependence of sulfur contents



(a)



(b)

Figure 5.8 Sulfur rich area obtained by (a) sulfur print for A106 Gr.B, and (b) EDS for SUM24L.

Chapter 6. Mechanism of LDIE Damage

6.1 Corrosion mechanism

In Chapter 5, the key factors of LDIE have been identified and the transition phenomenon has been discussed from the experimental data. In this chapter, the micro- and nano-structural morphology of the damaged specimens will be examined based on FE-SEM analysis. The main focus is to investigate the damage mechanism of LDIE. To examine the microstructural evolution of damage, understanding fundamental damage mechanism of LDIE is important.

To understand the initiation process of the LDIE damage and root cause of the initiation process, SEM analysis has been made on LDIE test specimens as a function of time. Figure 6.1(a) shows the surface within the pearlite grain of the damaged specimen after 30 minutes test for A106 Gr.B. There shows cavities due to iron dissolution on the pearlite grain and the small clusters of oxide precipitates were dispersed along lines. Iron oxides were identified as magnetite by XRD earlier. Figure 6.1(b) shows that it is clear that iron dissolves from the ferrite layers selectively and the lamellar structure of cementite layers was remained. From the SEM images, the initiation is shown to start from pearlite region. The cause for the selective dissolution phenomenon can be explained by galvanic action between cementite (acting as a cathode) and ferrite (acting as an anode) leading to an electrochemical cell.[72] Figure 6.2(a) and (b) also show that the initiation of damage starts at the pearlite region and narrow planer area between ferrite and pearlite is

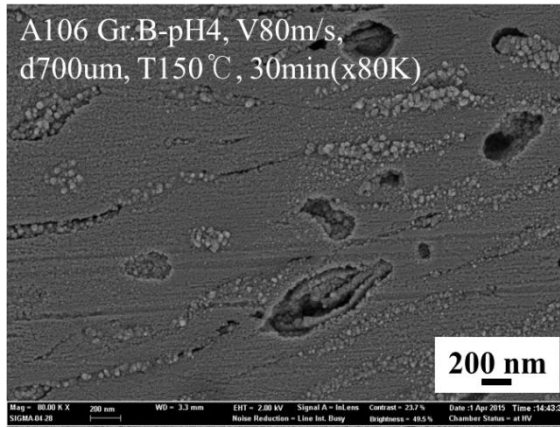
preferentially damaged. Figure 6.2(b) shows the damage initiates as a pit at the interface between ferrite and pearlite in lamellar pearlite region. However, the damage is not extended to cementite plates.

Figure 6.3 shows further evolution of LDIE damage due to droplet impingement. It is clear that a chunk of pearlite structure can be removed by the mechanical effect of impinged droplets when the corrosion damage is progressed to certain extent as shown in Figure 6.3(a). Chunks of pearlite fell out of the pearlite region clearly by impinged droplets. Figure 6.3(b) shows slightly different damage morphology of teared lamellar structure by the impinged droplets. It is evidence of erosion process as shown in the SEM results.

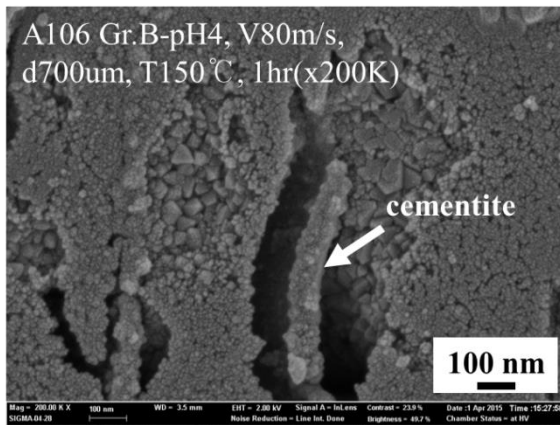
It is shown earlier that the initiation of damage is the selective dissolution of ferrite in the pearlite region. The damage evolves with accumulating the number of repetitive impingement of droplets. To examine the damage into the hole, the cross-sectional area has been examined by section specimens in vacuum by focused ion beam (FIB). As shown in a high resolution SEM image (x80K) in Figure 6.4(a), the damage path can be made by repetitive impingement which makes iron dissolve in wetted condition and easily fall out. Figure 6.4(b) was obtained by focused ion beam (FIB) inside FE-SEM system. The cross-sectional area between the ferrite and the pearlite shows that the delamination occurred in the pearlite region and the severe damage occurred in the phase boundary. The delamination is the results of selective dissolution of ferrite layers. The damage in the phase boundary showed that pearlite region is the weakest area for the initiation and propagation of

corrosion induced LDIE.

To investigate more details about damage sequence of events, destructive analysis has been conducted in the specimens where the original surface has been already removed in those specimens. The results will be described in next chapter 6.2.

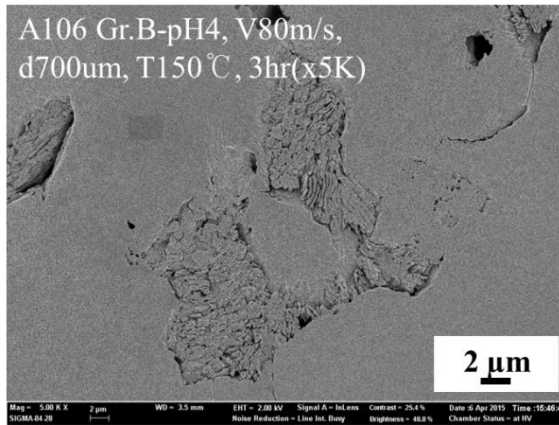


(a)

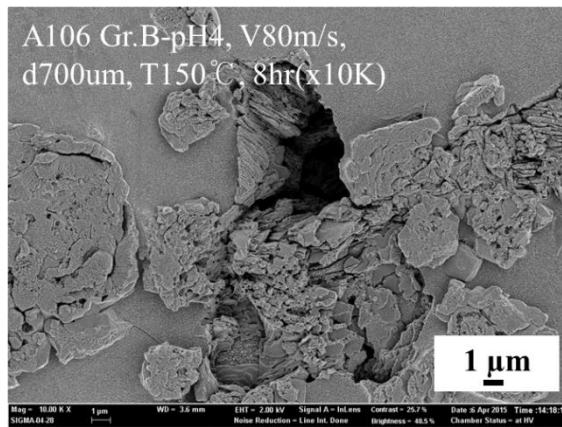


(b)

Figure 6.1 Initiation of LDIE damage(A106 Gr.B, pH 4, droplet velocity 80 m/s, droplet diameter 700 μm)-(a) cavities due to iron dissolution on pearlite, (b) the lamellar structure of cementite layers.

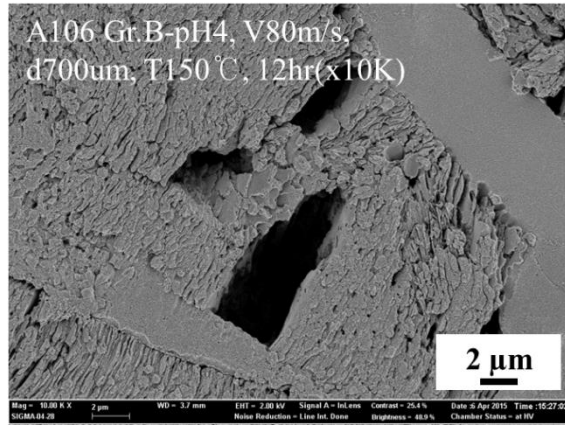


(a)

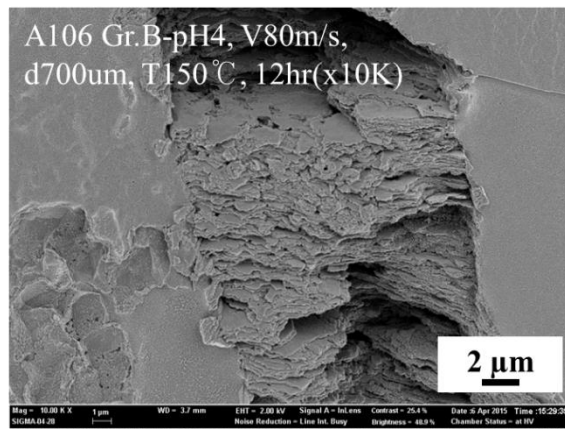


(b)

Figure 6.2 Initiation of damage(A106 Gr.B, pH 4, droplet velocity 80 m/s, droplet diameter 700 μm)-(a) pearlite corrosion and revealed grain boundary, (b) ferrite-pearlite grain boundary damage.

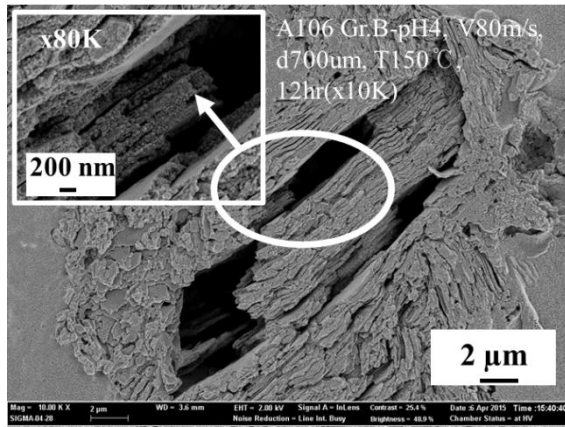


(a)

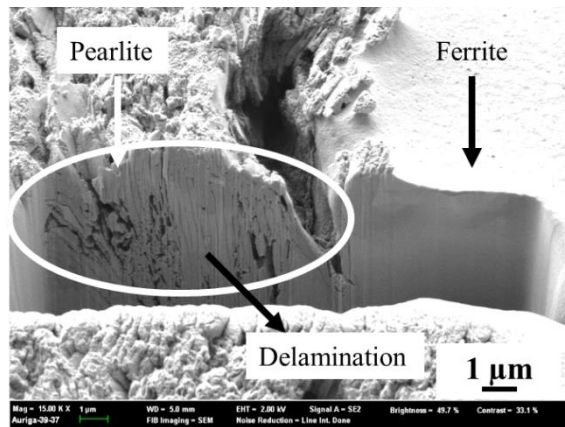


(b)

Figure 6.3 Local damage initiation(A106 Gr.B, pH 4, droplet velocity 80 m/s, droplet diameter 700 μ m)-(a) chunks of pearlite fell out of a pearlite region, (b) the lamellar structure teared by impinging droplets.



(a)



(b)

Figure 6.4 Local damage initiation(A106 Gr.B, pH 4, droplet velocity 80 m/s, droplet diameter 700 μm)-(a) damage path into the pearlite, (b) delamination of pearlite and ferrite-pearlite boundary damage (FIB).

6.2 Erosion mechanism

To investigate more details about damage sequence of events, FE-SEM analysis has been conducted in the specimen cross-section where the original surface has been already removed in those specimens. After the original surface is removed by the LDIE, the damage path is spread laterally on the surface. As explained in Chapter 5, it has been observed that: (i) there exists a transition point beyond which the damage rate rapidly increases; (ii) prior to the transition point, damage rate is lower as limited to surface; and (iii) after the transition period, a higher damage rate is accompanied by the removal of pearlite chunks.

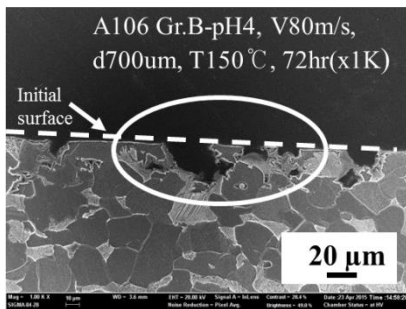
Near the transition, the tested specimens were observed metallographically. Figure 6.5 shows the cross-section of the damaged specimens, made of A 106 Gr.B. The specimen was mounted on epoxy resin and polished by using diamond suspension up to $0.1\ \mu\text{m}$. After 2% nital etched, the ferrite and pearlite region can be easily identified in the specimen. Relatively light region in the Figure 6.5 is pearlite.

In the Figure 6.5(a) and (c), the dotted white lines represent the original surface which is not damaged. In Figure 6.5(b) and (d) shows remained ferrites. The figures are corresponding to the previous results. The existence of ferrites and damaged region in the pearlite means that the weakest region is the pearlite.

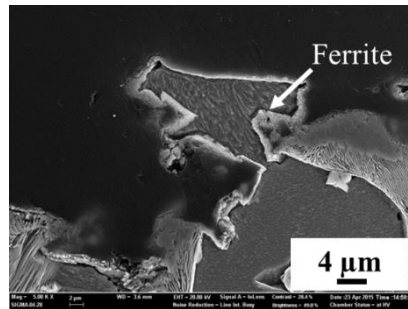
In addition, the initiation mechanism is selective dissolution of ferrite in the pearlite grains. During the transition, the damage depth is a few grain size of prior austenites. This can be a basis of determining the transition as a

physical meaning. It means that the transition period may be determined by the material microstructure, not the test time or impingement frequency. More detail discussion will be noted in Section 6.3.

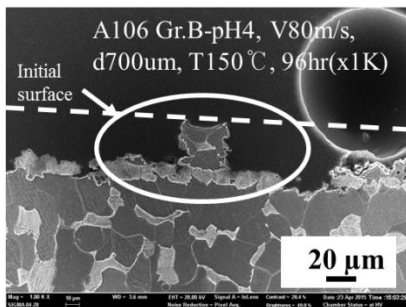
When the original surface has been removed, the morphology can be shown as Figure 6.6. In this case, about 120 hours of exposure in LDIE test is sufficient to remove original surface grains and reveal rough surface by damages on the surface. The damaged surface was roughened and the evidence of removal process has been shown in the chips which are between the epoxy resin and the damaged surface. The chips are lumps of ferrite which can be easily removed by impinged droplets. In this stage, the material mass loss is drastically increases. It means the damage mechanism is governed by mechanical erosion process.



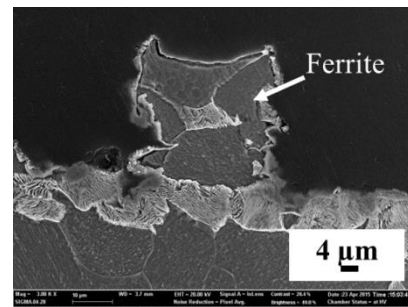
(a)



(b)

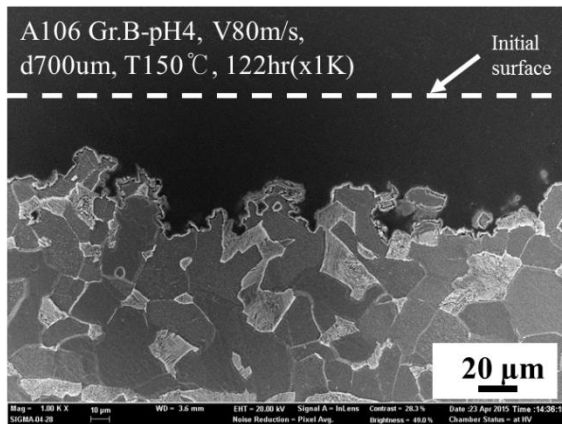


(c)

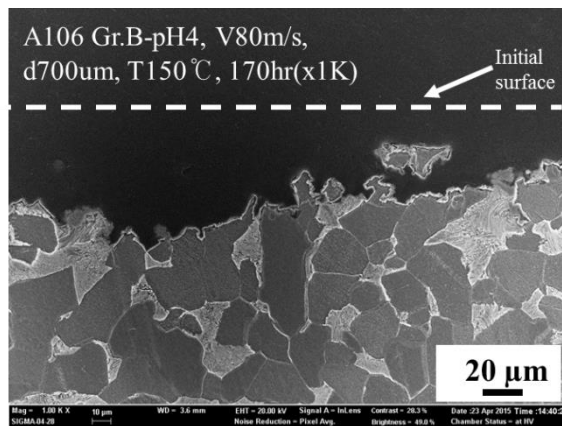


(d)

Figure 6.5 Cross-sectional investigation of the damaged specimen during transition period.



(a)



(b)

Figure 6.6 Cross-sectional investigation of the damaged specimen during stable-loss period.

6.3 Microstructural damage propagation process

In Section 6.2, the mechanisms of LDIE damage initiation and the transition to propagation were examined by the micro- and nano-structural analysis of accelerated test materials. The initiation of damage occurs at surface layer by the selective dissolution of ferrite layers in the pearlite region in which galvanic corrosion operates. Transition periods are found to vary with pH and liquid drop diameter, and are appeared to define the end of the initiation period of surface corrosion damage. The propagation damage occurs more rapidly into the pearlite grains after the original surface is removed by the transition. After the transition, erosion-dominated damage occurs because of removing ferrite chunks due to impinged droplets.

Therefore, the sequence of events for the LDIE in LAS can be illustrated by a sketch as shown in Figure 6.7. It assumes that ferrite (F) and pearlite (P) are distributed on the surface randomly. In the first, initiation stage (I-1), anodic dissolution of ferrite occurs on the pearlite leaving cementite plates behind. The lamellar structure of cementite layers is revealed. In the second initiation stage (I-2), chunks of pearlite are removed by repetitive impingement of liquid droplets and it leads extensive removal of surface grains. In the transition stage (T), the mass loss rate starts to increase with complete removal of surface grains. Detachment of the initial surface grains results in fractal topology that is more vulnerable to mechanical damage. Finally, in the propagation stage (P), detachment of large pieces of fractal structure occurs by the mechanical effect of impingement. The corrosion occurs simultaneously during the propagation period while erosion process

dominates damage in the stage (P). Finally, the process reaches a stable-loss propagation period in which the mass loss rate saturates to a constant value.

To test the reproducibility of the LDIE damage mechanism and the mass loss rate, selected specimens that had undergone different stages were re-polished specimen and tested again at the same conditions as the original tests. Figure 6.8 shows the re-test results confirming the reproducibility and consistency of the damage process. Therefore, the suggested mechanism and the features of the mass loss rate are suggested as the fundamental nature of the LDIE damage process.

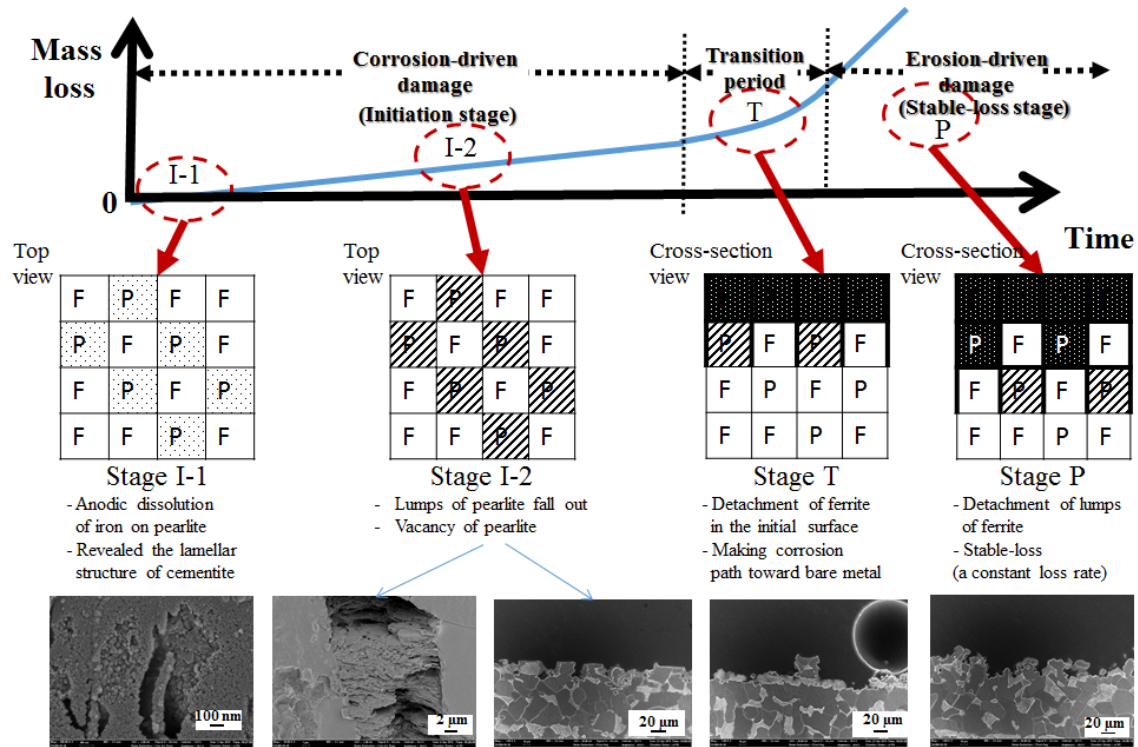


Figure 6.7 The schematic of sequence of events and damage mechanism.

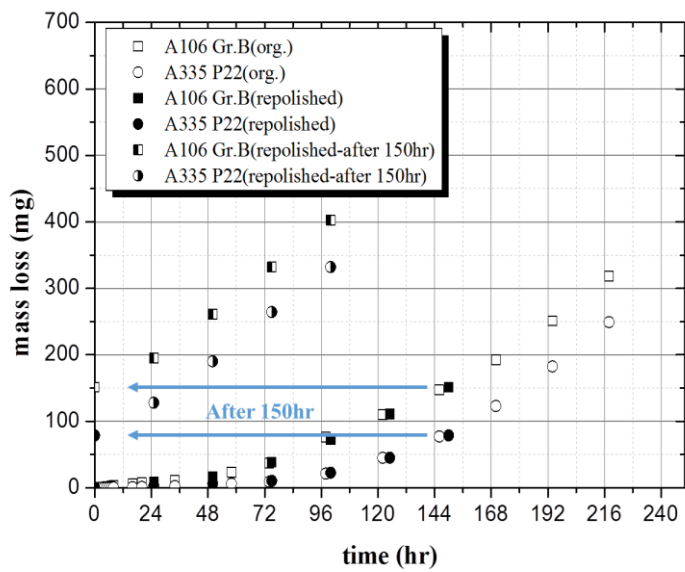


Figure 6.8 Reproducibility by a re-polish test.

Chapter 7. LDIE Prediction Model

7.1 Semi-empirical model for pipe wall thinning

One of the key objectives of this thesis is to develop a prediction model for the LDIE damage quantitatively. Based a database for accelerated tests, the mechanism and the functional dependence of the LDIE rate as determined before were utilized to develop a model. Especially, it is the first step to predict the transition time after which the damage rate accelerates by erosion-dominated process from the initial corrosion-dominated process.

Table 7.1 summarizes the transition time, t_{ce} , obtained from the microstructure and mass loss data. The transition time could not be defined at the high pH conditions (pH 4.5~5) due to the limitations in test durations. From the pH 4 data of Table 7.1, the mass loss up to the transition time per unit area has been calculated at each test condition for both A106 Gr.B and A335 P22. The results show that the accumulated mass loss per unit area up to the transition is nearly constant, regardless of droplet velocity and droplet size as shown in Figure 7.1. The accumulated mass loss per unit area can be defined as a critical mass which can be a representative value of transition period. By data analysis, the critical mass loss density is determined to be about 23mg/cm². Assuming the uniform damage on the surface, the mass loss can be shown to be equal to the average grain size of prior austenite. That is about 33 μ m in both materials. It implies that the transition can be defined as the time taken to remove the surface layer by one-grain depth.

To characterize the nature between the critical mass loss density and the transition time, a model for predicting transition time has been determined as shown in Figure 7.2(a). The time to reach the critical mass loss density is defined as a function of pH. As pH increases, the transition time increases exponentially. It is because the mass loss change is decreased by increasing the pH level. This result also explains how the ferrous ion solubility affects the LDIE damage rate. Figure 7.2(b) shows that the transition time is proportional to pH exponentially.

The relationship between the mass loss rate and key factors of LDIE is also explored. Figure 7.3 shows regression analysis results for the mass loss rate as function of key factors including droplet velocity, droplet size, magnetite solubility, etc. Comparing the initiation and the propagation stage, it can be shown the corrosion effect remains unchanged in both stages but the erosion effect becomes more pronounced at the propagation stage. It indicates that erosion process due to the mechanical effect such as droplet size and velocity is dominant in the final steady state damage period. It is clear that the key factors employed in the experimental design are indeed principal variables that control the LDIE damage rate.

To confirm the identified damage mechanism in each stage, published models have been employed to compare with the measured data. As the first step, the measured data of A106 Gr.B was compared with the models for corrosion and erosion rate prediction.

Sanchez-Caldera[68] improved Berge's model[73] to predict corrosion rate in flowing conditions in a pipe flow. The Sanchez-Caldera equation is

expressed as follows;

$$\frac{dm}{dt} = \frac{\theta(C_e - C_\infty)}{\frac{1}{k} + (1-f)\left[\frac{1}{h_D} + \frac{\delta}{D}\right]} \quad \text{Eq. (7.1)}$$

where

C_e : equilibrium concentration of iron, kg/m^3 ,

C_∞ : iron species concentration in bulk water, kg/m^3 ,

θ : oxide porosity(0~1.0),

k : reaction rate constant, m/s ,

f : fraction of oxidized metal converted into magnetite at the metal-oxide interface,

h_D : mass transfer coefficient,

Δ : oxide thickness, m ,

D : diffusion coefficient of the dissolved ferrous species, m^2/s .

Sanchez-Caldera improved Berge's model[73] which is derived as follows;

$$\frac{dm}{dt} = k(C_s - C_\infty) \quad \text{Eq. (7.2)}$$

where

C_s : ferrous ion concentration at the oxide/water interface, kg/m^3 .

The other parameters of Berge's model are same with those of the Sanchez-Caldera's model. The originality of Sanchez-Caldera's model lies in the addition of the effect of oxide thickness and its porosity into the model.

Basically, the solubility of magnetite determines the corrosion rate in flowing water. Therefore, in Sanchez-Caldera's model, the terms including mass transfer coefficient and oxide thickness are less important. Consequently, Sanchez-Caldera's model can be simplified into a form that is dependent only on the solubility; i.e. back to Berge's model.

Key differences between the Berge's model and the measured data of the LDIE test can be explained as follows. In flowing conditions, the LDIE test was conducted for water droplets impinging to the normal direction of a material while the Sanchez-Caldera's model assumes that the flowing direction of water is parallel to the material. Hence, contact time in LDIE is an actual duration material is washed by liquid droplets. Therefore, a correlation is made on time by comparing the measured results with the equivalent calculation results by using the Berge's model.

Considering above assumptions, the result of Berge's model with modified parameters was calculated and its result was compared with the measured data of the LDIE test. Figure 7.4(a) shows the relationship between Sanchez-Caldera model and the measured data of A106 Gr.B. The relationship between the measured data and the Sanchez-Caldera's model result is linear on a log scale.

A slope of correlation is about 0.98 with 0.11 for standard error. An intercept is about 0.72 on the logarithmic scale that correspond to about 5 on a linear scale. It means that the measured data is about 5 times larger than the model result. In terms of damage mechanism, the correlation of Figure 7.4(a) shows that the measured data of the LDIE test is strongly dependent on the

solubility of magnetite. From the r-square value[74] (0.89), the model has fairly good correlation with the measured data.

For the prediction of propagation, the Isomoto's erosion model is employed.[52] Figure 7.4(b) shows the relationship between the Isomoto's model and the measured data of A106 Gr.B. Isomoto[52] derived a LDIE prediction model on the mass loss rate based on experimental study while taking into account erosion effects as follows;

$$\frac{dm}{dt} = C_0 H v^{-2.75} F_{freq} m_l V^2 \quad \text{Eq. (7.3)}$$

where

C_0 : a constant,

Hv: material hardness, GPa,

F_{freq} : number of impinged droplets per unit area and time, #/mm²sec,

m_l : mass of a droplet, kg,

V: the impingement speed of the droplets, m/s.

The Isomoto's model is focused only the erosion effect while ignoring oxide/corrosion effect. This is because the model was based on the experimental data of high velocity impingement of liquid droplet at room temperature[52]. The model describe that the damage rate is dependent on kinetic energy of a droplet. In the Isomoto's model, the impinging frequency and material resistance against impinging droplets is important to predict the

mass loss rate.

As shown in Figure 7.4(b), the measured data and the Isomoto's model result correlate well on a log scale. The slope of the linear correlation is determined by regression to be about 1.19 with a standard error of 0.21. An intercept of 0.002 confirms a fair correlation. The derived correlation shows that the measured data after transition is linearly proportional to the kinetic energy of droplets, *i.e.* $\frac{1}{2}mV^2$. Finally, all of the measured data of A106 Gr.B were employed in the model building for corrosion and erosion rate prediction as shown in Figure 7.4.

To test the validity of the derived LDIE prediction model, the model has been compared all of the measured data obtained the test materials including A106 Gr.B, A335 P22, and SUM24L. The results have been shown in Figure 7.5. The correlation of Figure 7.5(a) is corresponding with that of Figure 7.4(a). It shows that the mass loss rates are consistently dependent on the solubility of magnetite in the initiation stage for all materials. The slope of correlation is determined by regression to be about 1.04 with the standard error of 0.1. The intercept on the log scale is about 0.84 that corresponds to about 7 on a linear scale. It means that the measured data on the mass loss rate is about 7 times greater than the model prediction. The r-square value (0.83) is similar with the r-square value in Figure 7.4(a) (0.89). In Figure 7.5(b), the slope of correlation (1.196) is nearly same with the slope of Figure 7.4(b) (1.192). The r-square value is 0.57 lower than the value of Figure 7.4(b) (0.86). Therefore, it is believed that there is systematic error in the material

resistance factor, because the value is based on experimental results. The correction factor, $1/7$ has been applied to fit to the database.

In order to investigate alloying effects on the LDIE damage, test materials with different chemical compositions were chosen. Especially, in the initiation stage, the corrosion is the dominant mechanism initiating the LDIE. In this thesis, alloying effects on the corrosion are examined based on literature studies, because material compositions in this thesis are not adequately covered to systematically examine the alloying effects.

Al-Hassan et al.[74] measured the static corrosion rate of steels in water containing carbon dioxide as shown in Figure 7.6(a). As the carbon dioxide content increases, the corrosion rate also increases at same temperature. It has been known that cementite (Fe_3C) is nobler than ferrite and therefore has a lower over-potential for hydrogen evolution[74]. It is shown that micro-galvanic cells can be formed between cementite and ferrite layers within pearlite, resulting in selective attacks on ferrite and around pearlite regions.[72] Heitmann[43] investigated that the influence of Cr+Mo content on erosion-corrosion of LAS based on experiments at KWU as shown in Figure 7.6(b). As the Cr+Mo content increases, the corrosion rate drastically decreases.

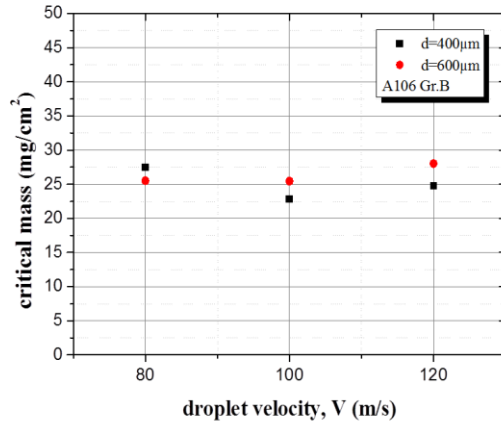
A rudimentary analysis on alloying effects for corrosion has been made on Cr and Mo in this thesis. Figure 7.7 shows the alloying effects on the mass loss rate. The mass loss rate in the Figure 7.7 is the rate in the initiation stage. In Figure 7.7(a), except A335 P22, as carbon content of the materials increase, the mass loss rate increases. In Figure 7.7(b), the dependence of the Cr+Mo

content is not evident in all material except A335 P22. From the results, it is supposed that the Cr+Mo effect is not important in LDIE for the range of materials examined.

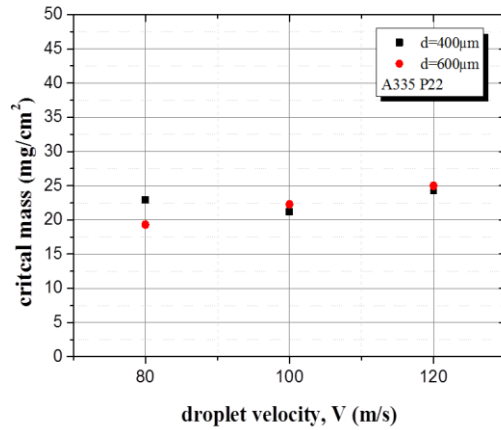
Considering the results from Figure 7.1 to Figure 7.5, the prediction model is predicted for entire period on the accumulated mass loss density with time for LAS under LDIE as described in Figure 7.8.

Table 7.1 Transition time, t_{ce} obtained from microstructure and mass loss data

Test (#)	V (m/s)	pH	D (μ m)	t_{ce} (hr)	
				A106 Gr.B	A335 P22
#1	120	4	600	48	72
#2	80	4	600	96	96
#3	80	5	600	-	-
#4	120	5	600	-	-
#5	80	4.5	600	-	-
#6	120	4.5	600	-	-
#7	100	4	600	48	72
#8	80	4	400	72	96
#9	100	4	400	48	72
#10	120	4	400	48	72

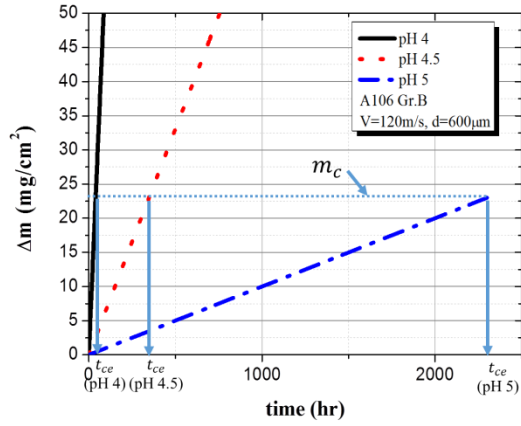


(a)

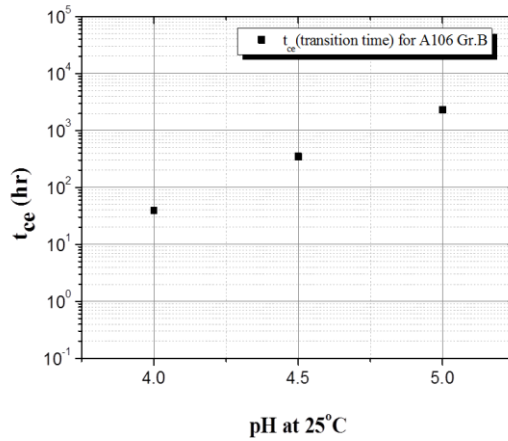


(b)

Figure 7.1 Critical mass loss-(a) critical mass for A106 Gr.B(black square for 400 micrometer-droplet size, red circle for 600 micrometer-droplet size), (b) critical mass for A335 P22(black square for 400 micrometer-droplet size, red circle for 600 micrometer-droplet size).

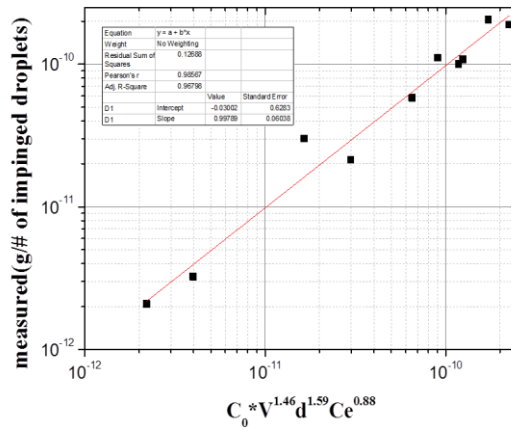


(a)

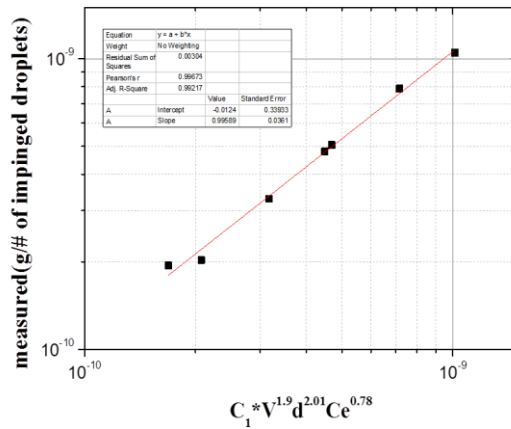


(b)

Figure 7.2 Calculated transition time-(a) transition time as determined by the critical mass, (b) transition time as a function of pH.

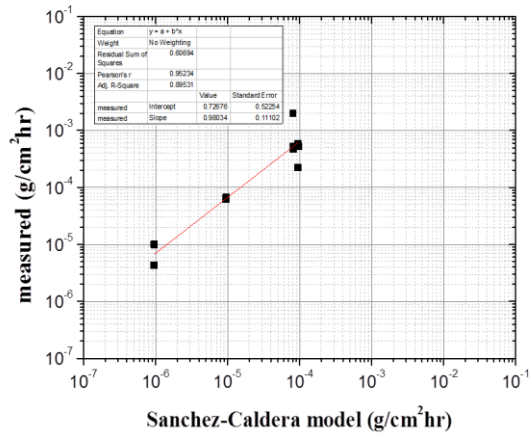


(a)

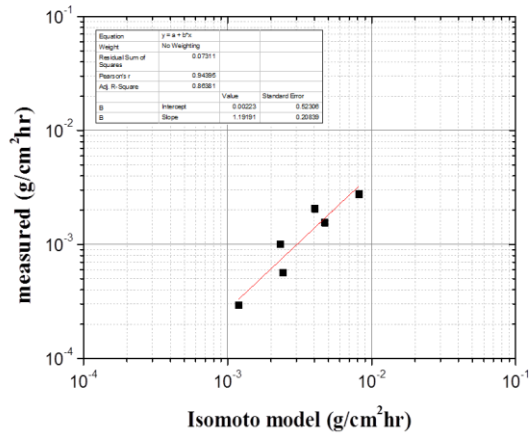


(b)

Figure 7.3 Regression results and relationship between the mass loss rate and the key LDIE factors including the magnetite solubility C_e , the droplet velocity, V and the droplet diameter, d -(a) initiation stage, (b) stable-loss stage(after transition time).

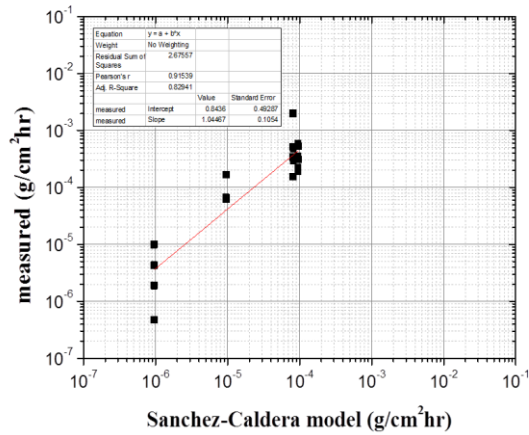


(a)

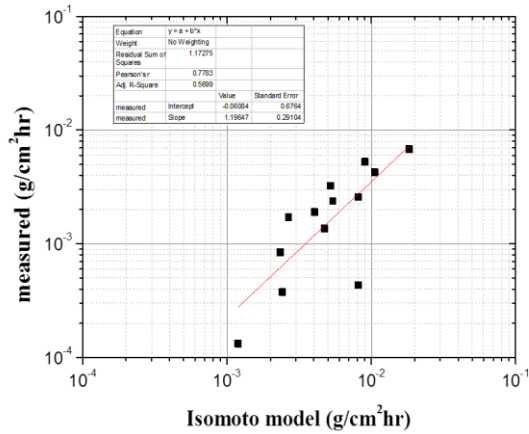


(b)

Figure 7.4 Comparison of measured data and the Sanchez-Caldera model(for A106 Gr.B)- (a) initiation stage, (b) stable-loss stage(after transition time).

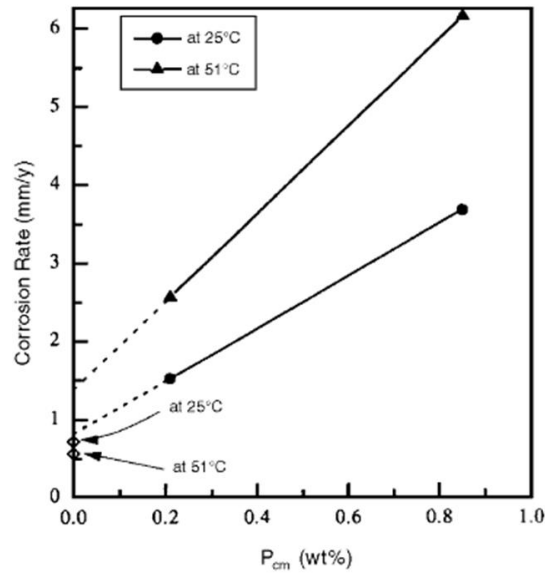


(a)

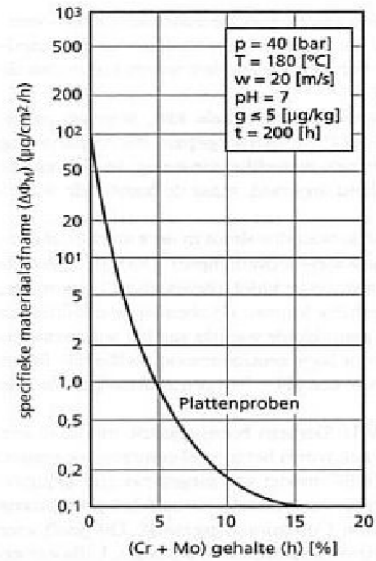


(b)

Figure 7.5 Comparison of measured data and the Sanchez-Caldera model for all test materials including A106 Gr.B, A335P22, and SUM24L -(a) initiation stage, (b) stable-loss stage(after transition time).

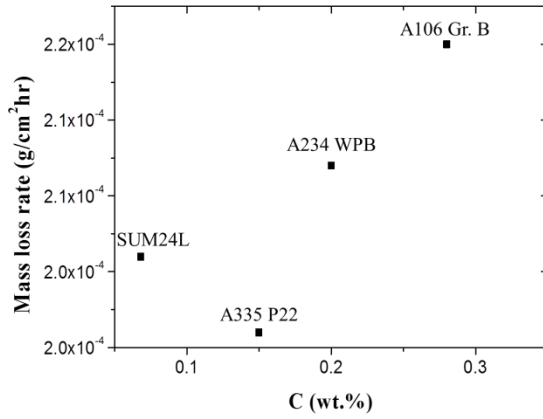


(a)

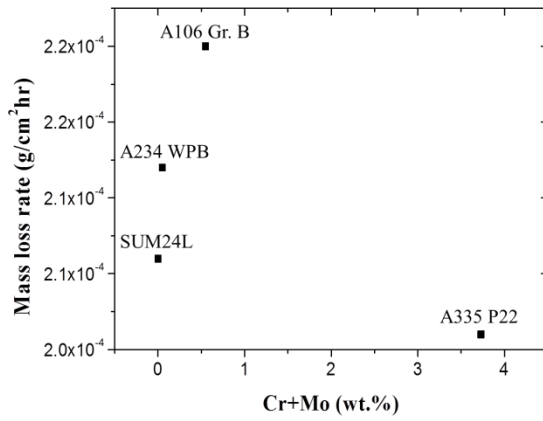


(b)

Figure 7.6 Material dependence of corrosion rate-(a) corrosion rate as a function of carbon content in steels[74], (b) Influence of Cr+Mo content on erosion-corrosion according to the experiments of KWU[43].



(a)



(b)

Figure 7.7 Mass loss rate of LAS as a function of alloying contents-(a) carbon contents, (b) Cr and Mo contents.

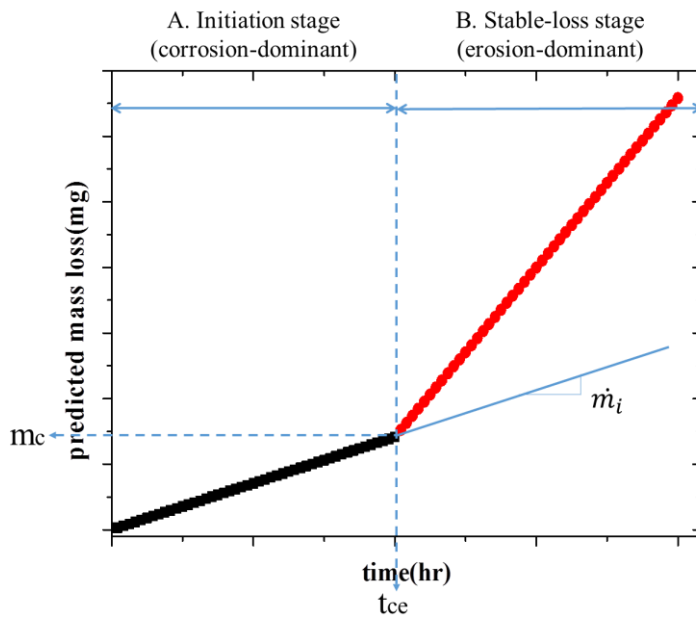


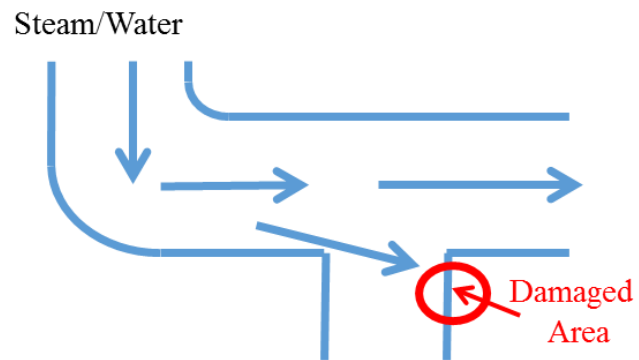
Figure 7.8 The schematic of developed model which is a bi-linear model including the corrosion-dominant initiation stage and the erosion-dominant stable-loss stage.

7.2 Model benchmark with field data

To verify the developed model, a benchmark study has been conducted using single data point obtained from the field experience. The field data for the secondary side of a PWR was provided by KEPCO E&C[75]. In the field conditions, the droplet size was determined by Tatterson[76] correlation assuming that all of the flowing water can be changed to droplets. The droplet number density per unit area and time is calculated to be $1.86 \times 10^7 \#/\text{cm}^2\text{hr}$. The field material is A234WPB which has similar chemical composition with A106 Gr.B. The damaged section is a line from high pressure (HP) turbine to moisture separator re-heater (MSR) as sketched in Figure 7.9. The main pipe diameter is 1.2 m flowing with steam/water flow. The details are given in Table 7.2, and Table 7.3.

From the prediction result of the developed model, corrosion and erosion dominant regions are defined as shown in Figure 7.10. The initial stage in which the original surface was removed predicted to take about 5000hr, equivalent to about 0.6 year. After the transition, the stable-loss stage to failure is predicted to take about 11.8 years. The predicted failure time is about 65% of the field failure time. It means the model over-estimate the damage rate. One of the uncertainties is attributed to the number density of droplets. It is very conservative condition to assume all flowing water transform to droplets. The accuracy of predicted value needs to be further tested with more data.

Damaged section: a line from HP turbine to MSR (48" pipe to 20" pipe)



(a)



(b)

Figure 7.9 Field failure case-(a) schematic of the damaged section, (b) photograph of the damaged area[4].

Table 7.2 Field failure case-operation conditions and droplet properties[75].

Initial thickness	Droplet velocity	Droplet size	Temperature	Hot pH	Quality	Mass flow rate(water)	Flow area	Droplet density
mm	m/s	mm	°C			kg/hr	cm ²	#/cm ² hr
8	51.87	1.2	173	6.26	0.868	136368	8103.21	1.86e+07

Table 7.3 Field failure case-material composition.

	C	Si	Mn	P	S	Cu	Ni	Cr	Mo	σ_y
	wt. %									MPa
A234 WPB	0.3	0.1	0.29-1.06	0.05	0.1	0.4	0.4	0.4	0.15	240

Table 7.4 Predicted results using a field failure case assuming the number density of impinging droplets as $1.86 \times 10^7 \#/\text{cm}^2\text{hr}$.

Operation time	Field thinning rate	Prediction model	Prediction model	Prediction model	Prediction model	Time to failure	Prediction /Field
		initiation	stable-loss	initiation	stable-loss		
hr	mm/hr	mm/hr	mm/hr	hr	hr	hr	%
167107	4.78e-05	5.7e-06	8.0e-05	5592	104163	109756	65.68

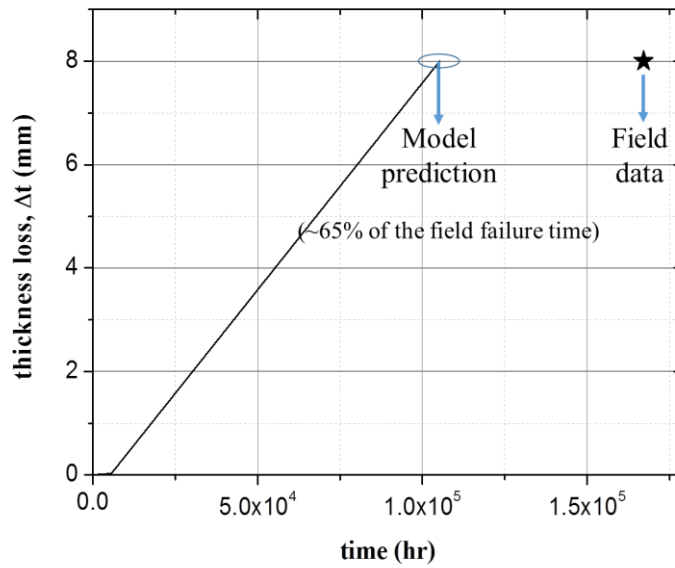


Figure 7.10 Comparison of the failure time and the model prediction result that is equal to 65%(about 12 yrs.) of the field failure time.

Chapter 8. Conclusions

8.1 Conclusions

The liquid droplet impingement erosion (LDIE) phenomenon in the secondary side of PWRs has been investigated in this thesis in order to understand fundamental mechanism and to develop the prediction model in support of the long-term operation of nuclear power plants. The principal questions that are answered in this thesis include; (i) what is the fundamental damage mechanism of LDIE in the secondary side of PWRs? and (ii) how can we predict the damage quantitatively?.

From the literature review, it has been found that most of published models on LDIE do not explain interaction mechanisms between liquid drops and materials. Difficulties in studying mechanisms arise from the fact that it requires; (i) acceleration testings of the phenomenon in mechanistically relevant environments; and (ii) identifications of detailed micro- and nano-structural process responsible for the phenomenon with functional dependence on key factors.

The key factors influencing LDIE have been identified and an acceleration test method has been developed in this thesis. In order to accelerate the LDIE phenomenon, the experiments have been conducted under reducing environment with lowering the pH level. The rotating disc test method has been successfully developed to accelerate the LDIE damage by controlling droplet velocity and size to get enough mechanical impacts in relevant water

chemistry. In this thesis, three types of low-alloy steels were employed to investigate the effect of microstructure and chemical composition. Investigated materials have chemical compositions, especially carbon, sulfur, and chrome , to examine the effect of microstructural and mechanical properties.

According to the test matrix, the experimental tests have been conducted for a period up to 200 hrs. The mass loss rates were measured as functions of pH, droplet velocity, and droplet size, quantitatively. From the experimental results, it was confirmed that the identified key factors are strongly correlated with the LDIE damage rates. In addition, it was found that there is a distinct transition period in which the LDIE mechanism changed for corrosion to erosion.

To understand fundamental damage mechanism of LDIE in detail, the micro- and nano-structural analysis has been examined. From the microstructure analysis, the sequence of events during the LDIE damage test has been identified. The initiation of damage occurs at surface layers by the selective dissolution of ferrite layers in the pearlite region in which galvanic corrosion operates between ferrite and cementite.

Transition periods are found to vary with pH and liquid drop diameter, and are appeared to define the end of the initiation period of surface corrosion damage. The propagation damage occurs more rapidly into the pearlite grains after the original surface is removed by the transition. After the transition, erosion-dominated damage occurs by removing ferrite chunks due to the mechanical effect of impinged droplets.

To predict the LDIE damage rate quantitatively, a semi-empirical model has been developed in this thesis. The mechanism and database of the damage rate as determined were utilized to develop the model. The model first predicts the transition time at which the damage rate thereafter accelerates by erosion-dominated process for the initial corrosion-dominated process based on the average size of the prior austenite grains in LAS. The accumulated mass loss per unit area up to transition can be defined as a critical mass which can be a representative value of transition period. It was found that the critical mass is not dependent on affected factors but material microstructure.

To confirm the validity of developed model, published models which are suggested by Sanchez-Caldera and Isomoto, respectively, have been employed to compare with the measured data. The correlation of initiation data shows that the measured data of the LDIE test is strongly dependent on the solubility of magnetite. The derived correlation shows that the measured data after transition is indeed proportional to the kinetic energy of droplets.

Finally, a bi-linear prediction model has been proposed, as functions of time, pH, and water droplet momentum to delineate the corrosion-induced period and the erosion-dominating period as follows;

(i) Initiation stage

$$\dot{m}_i = C_0 \cdot C_{e,magnetite} \cdot A \cdot f(t) \cdot f(T) \quad \text{Eq. (8.1)}$$

where \dot{m}_i is mass loss rate for initiation ($\text{g}/\text{cm}^2\text{hr}$), C_0 is a constant, $C_{e,magnetite}$ is magnetite solubility (g/m^3), A is the fraction of wetted

area($0 < A \leq 1$), $f(t)$ is the fraction of effective time which is the ratio actual impinged time to tested time($0 < f(t) \leq 1$), $f(T)$ is temperature function(1 for 150°C).

(ii) Propagation (stable-loss) stage

$$\dot{m}_{SL} = C_1 \cdot F_{freq} \cdot m_d \cdot V_d^2 \cdot Hv^{-2.75} + \dot{m}_i \quad \text{Eq.(8.2)}$$

where \dot{m}_{SL} is mass loss rate for stable-loss ($\text{g}/\text{cm}^2\text{hr}$), C_1 is a constant, F_{freq} is the number density of impinging droplets($\#/\text{cm}^2\text{hr}$), m_d is mass of a droplet (g), V_d is droplet velocity(m/s), Hv is Vickers hardness (GPa).

To verify the developed model, the model was applied to predict one known case of a field failure. It is found that the developed model under-predict the failure time by about 30%. The calculated result is the most conservative result with $1.86 \times 10^7 \#/\text{cm}^2\text{hr}$ of droplet number density. There is an uncertainty because of droplet number density prediction. Nevertheless the developed model prediction is shown to estimate the failure time reasonably.

8.2 Future work

This research is the first attempt to clarify the LDIE damage mechanism by relevant accelerated experiments in the environments of the secondary side of PWRs. The usefulness of the developed model has been demonstrated by comparing with available field data.

However, the field conditions are more complex in the PWR secondary components compared with other industries. For an example, some of pipes or fittings in the PWR secondary side contain solid particles that can affect to the damage of structural materials. Therefore, it is needed to add the multi-phase erosion prediction model for more reliable prediction.

In addition, the data base used in the model development was derived from short-term experiments under highly accelerated condition by lowering pH as presented in Appendix A1. Longer tests at higher pH including neutral water condition deserve for further studies. It is also recommended to verify the temperature dependence of LDIE by conducting tests at various temperatures.

References

- [1] U.S.NRC, Expert Panel Report on Proactive Materials Degradation Assessment (NUREG/CR-6923) 2007, U.S. Nuclear Regulatory Commission.
- [2] Tipping, P. G., “Understanding and Mitigating Ageing in Nuclear Power Plants”, Woodhead Publishing, (2010).
- [3] Shah, V. N. and Macdonald, P. E., “Aging and life extension of major light water reactor components”, Elsevier (1993).
- [4] KEPCO E&C maintenance database.
- [5] EPRI, Recommendations for controlling cavitation, flashing, liquid droplet impingement, and solid particle erosion in nuclear power plant piping systems (TR-1011231) 2006, EPRI.
- [6] Finnie, I., “Erosion of surface by solid particles”, *Wear* 3 (1960), pp. 87-103.
- [7] Bitter, J. G. A., “A Study of erosion phenomena-Part I” *Wear* 6(1963), pp.5-21.
- [8] Bitter, J. G. A., “A Study of erosion phenomena-Part II” *Wear* 6(1963), pp.169-190.
- [9] Kosel, T. H., Solid particle erosion, friction, lubrication and wear technology. ASM handbook 18, ASM International 1992, pp.199-213.
- [10] Lynn, R. S., *et al.*, “On the particle size effect in slurry erosion”, *Wear* 149 (1991), pp. 55-71.
- [11] ASTM, “Standard terminology relating to wear and erosion”, G40,

Annual book of ASTM Standards, ASTM.

- [12] Gardner, G. C., "Events leading to erosion in the steam turbine", Proc. Inst. Mech. Eng. 178, (1966), pp 593-623.
- [13] Pearson, D., "Turbine blade erosion rig research and development work carried out at brighton," CEGB report RD/M/N41(43123), 1962.
- [14] Krzyaannowski, J. A. *et al.*, "Experience in Predicting Steam Turbine Blade Erosion," Proc. of 7th Int. Conf. on Erosion by Liquid and Solid Impact, (1987) pp.1-7.
- [15] EPRI, Interim Recommendations for an Effective Program Against Erosive Attack (TR1015071), 2007, EPRI.
- [16] Hirotsu, M., "Cavitation damage mechanism and its correlation to physical properties of material," ASTM STP 474 (1970), pp.48-66.
- [17] Heymann, F. J., "Toward quantitative prediction of liquid impact erosion" ASTM STP 474 (1970), pp.212-248.
- [18] Lesser, M., "Thirty years of liquid impact research: tutorial review," Wear 186-187 (1995) pp.28-34.
- [19] Fujisawa, N. *et al.*, "Critical consideration on wall thinning rate by liquid droplet impingement erosion," E-Journal of Advanced Maintenance 4(2012) pp. 79-87.
- [20] U.S.NRC, Erosion/Corrosion-induced Pipe Wall Thinning in US NPPs," NUREG-1344 (1987), U.S.NRC.
- [21] EPRI, "Nuclear Reactor Piping Failures at US Commercial LWRs:1961-1997," TR-110102 (1998).
- [22] EPRI, "Flow-accelerated corrosion in power plants," TR-106611 (1996).

- [23] T. Shoji, Workshop on Materials Innovation for Nuclear Optimized Systems, Dec. 5-7, 2012 CEA-INSTN Saclay , France.
- [24] Source from <http://tpowertec.com/Nuclear-STPP.htm>.
- [25] Heymann, F. J., “High speed impact between a liquid drop and a solid surface”, J. Appl. Phys., 40 (1969), pp.5113-5122.
- [26] Brunton, J. H., “Deformation of solids by impact of liquids at high speeds”, STP 307, ASTM (1962), pp 83-98.
- [27] Bowden, F. P., “The deformation of solids by liquid impact at supersonic speeds,” Proceedings of the Royal Society of London Series A, mathematical and Physical Sciences, (1961), pp.433-462.
- [28] Heymann, F. J., “Liquid impingement erosion,” ASM handbook 18:Friction,Lubrication, and Wear Technology (1992), pp.221-232.
- [29] Bramfitt, B. L., “Metallographer’s guide: practice and procedures for iron and steels, (2002) p. 2.
- [30] Field, J. E., Proc. of 6th Int. Conf. on Erosion by Liquid and Solid Impact, (1983) pp. 21-37.
- [31] Hattori, S., “Effect of impact velocity and droplet size on liquid impingement erosion,” ISAMM (2010), pp.58-71.
- [32] Hoff, G. *et al.*, “Material destruction due to liquid impact”, ASTM STP 408 ,(1966) pp 42-69.
- [33] Baker, J. *et al.*, Phil. Trans. A, 260, (1966) pp193-203.
- [34] Haller, D., Schweizerriche Bauzeithung, 101 (1933), pp 243-260.
- [35] Thiruvengadam, A., “The concept of erosion strength”, Hydronautics Inc. TR-233-9 (1966).

- [36] Rao, V. *et al.*, “Empirical relations for cavitation and liquid impingement erosion process”, NASA TR-2339 (1984).
- [37] KEPCO E&C, chemical analysis report.
- [38] Brush, E.G. *et al.*, “Corrosion and corrosion product release in neutral feedwater”, *Corrosion* 28, (1970), pp129-136.
- [39] Koshizuka, S. *et al.* International symposium on the aging management & maintenance of nuclear power plants(2010) 18-28
- [40] Karrab, S. A. *et al.*, “Study of cavitation erosion pits on 1045 carbon steel surface in corrosive waters”, *Journal of Tribology* 134, (2012), pp22-26.
- [41] Cragolino, G. *et al.*,”Review of erosion-corrosion in single-phase flows”, NUREG/CR-5156, ANL-88-25, US NGC (1988).
- [42] Bouchacourt, M., and Remy, F. N., (1991), Proceeding of 3rd NACE international Region Management Committee Symposium, Cambridge, U.K.
- [43] Heitmann, H. G. and Kastner, W., “Erosion-corrosion in water-steam cycles-causes and counter measures,” *Kraftwerkstechnik* 62, (1982), pp. 211-219.
- [44] NASA CR-1288, “Experimental and analytical investigations on multiple liquid impact erosion” (1969).
- [45] Honegger, E., “Tests on erosion caused by jets”, *Brown Boveri Review* 14, (1927) pp95-101.
- [46] Fyall, A. A., “A unified relation for cavitation erosion”, *Int. J. Mech. Sci.* Vol. 26, No. 5, pp. 325-335 (1984).
- [47] Adler, W. F., “The Mechanics of liquid impact”, *Treatise on Materials*

- Science and Technology”, Vol. 16. Erosion, pp. 127-183 (1979).
- [48] Thiruvengadam, A., “Handbook of cavitation damage”, Hydronautics Inc. TR-238-8 (1965).
- [49] Plesset, H., “Predictive capability of long-term cavitation and liquid impingement erosion models”, *Wear* 94, pp 259-274 (1984).
- [50] Heymann, F. J. *et al.* “Erosion by cavitation or impingement, ASTM Spec. Tech. Publ. 408,p. 70 (1967).
- [51] Miyata, H. *et al.*, “Erosion phenomenon caused by water droplet impingement and life prediction of industrial materials-Part 1”, *Ziryo-to-Kankyo* 57, (2008), pp. 138-145.(in Japanese).
- [52] Isomoto, Y. *et al.*, ““Erosion phenomenon caused by water droplet impingement and life prediction of industrial materials-Part 1”, *Ziryo-to-Kankyo* 57, (2008), pp. 146-152.(in Japanese).
- [53] Okada, H. *et al.* , “Evaluation methods for corrosion damage of components in cooling systems of nuclear power plants by coupling analysis of corrosion and flow dynamics(V)flow -accelerated corrosion under single- and two-phase flow conditions”, *Journal of Nuclear Science and Technology* 48, (2011), pp.65-75.
- [54] Ikohagi, T. *et al.*,”Advanced wall thinning prediction of liquid droplet impingement erosion”, *International Symposium on the Ageing Management & Maintenance of Nuclear Power Plants(ISaG2010)* (2010), 47-57.
- [55] Ikohagi, T., “On evaluation of LDI erosion rate based on fluid/solid coupled simulation”, *The 8th International Conference on Flow*

- Dynamics (ICFD2011), (2011).
- [56] Rajahram, S. S. PhD thesis, Univ. of Southampton (2010).
- [57] Dasgupta, R., “Effects of sand concentration on slurry erosion of steels,”
Material Transactions 39, (1998), pp.1185-1190.
- [58] Burstein, G. T., “Effect of impact angle on the slurry erosion-corrosion of
304L stainless steel,” Wear 240 (2000), pp.80-94.
- [59] Koshizuka, S. *et al.*, “Evaluation procedures for wall thinning due to flow
accelerated corrosion and liquid droplet impingement,” ISAMM (2010)
pp.18-28.
- [60] Nitoh, M. *et al.*, “Evaluation method for pipe wall thinning due to liquid
droplet impingement,” Nuclear Engineering and Design 264 (2013),
pp.195-202.
- [61] Campbell, F. C., “Elements of metallurgy and engineering alloys,” ASM
(2008).
- [62] ASTM, Standard test method for liquid droplet impingement erosion
using rotating apparatus, G 73-10.
- [63] ASTM, Standard test method for cavitation erosion using vibratory
apparatus, G 32-09.
- [64] ASTM, Standard test method for erosion of solid materials by a
cavitating liquid jet, G 134-95.
- [65] Oka, Y. I., *et al.*, “Effective parameters for erosion caused by water
droplet impingement and applications to surface treatment technology,”
Wear 263 (2007) pp. 386-394.
- [66] NASA CR-1288, “Experimental and analytical investigations on multiple

- liquid impact erosion” (1969).
- [67] ASME Sec. VIII Div.1.(1982).
- [68] Sanchez-Caldera, L. E., PhD thesis, MIT, (1984).
- [69] Sweeton, F. H. and Baes, C. F., “The solubility of magnetite and hydrolysis of ferrous ion in aqueous solutions at elevated temperatures,” J. Chem. Thermodynamics 2, (1970) pp.479-500.
- [70] Shimadzu Corp. Instruction Manual(AUW220D).
- [71] HSC Chemistry Ver.5.0, User Manual.
- [72] Revie, R. W. and Uhlig, H. H., “Corrosion and corrosion control,” (2008) p.143.
- [73] Berge, P. *et al.*, “Effects of chemistry on corrosion-erosion of steel in water and wet steam,” Water chemistry of nuclear reactor system BNES(Bournemouth: Oct. 1980) pp. 15-19.
- [74] Al-Hassan, S. *et al.*, “Effect of microstructure on corrosion of steels in aqueous solutions containing carbon dioxide,” Corrosion 54(6) (1998), pp.481-490.
- [75] Private communication with Dr. Hwang, K.M.
- [76] MOTIE, technical report, “Development of liquid droplet impingement erosion diagnostic system for carbon steel piping,” (2013).

Appendix

A1. Mass loss database of LDIE acceleration test

In this thesis, in order to accelerate the LDIE phenomenon, the experiments have been conducted under reducing environment with lowering the pH level. The pH level is in the range of 4 to 5 at 25 °C Table A1.1 summarizes the accumulated mass loss data obtained by each LDIE test. The test number of Table A1.1 is corresponding to the previous Table 4.2. The test duration was kept at 96 hours in each test condition. Four specimens were tested simultaneously for both A106 Gr.B and A335 P22. The mass loss was measured by removing specimens at the end of each 24 hours following the test procedures. In test conditions, dissolved oxygen level was maintained less than 5 ppb. And the temperature of water droplet sprayed to specimen is kept at 150 °C.

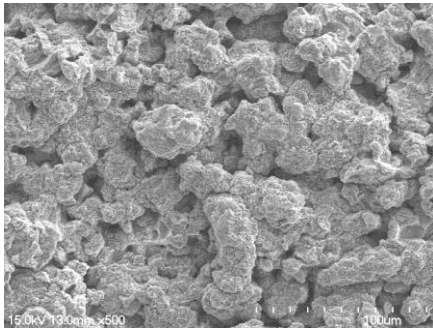
Mass loss rate per unit area and unit time can be measured by the actual impinged area, 14 mm x 15 mm and test time. In this test, impinged droplet density can be derived by photograph of impinged droplets and the impinging frequency. From the mass loss data of the LDIE tests, it is found that there is a transition point at a specific time where the mass loss rate changes to higher orders. As discussed, the mass loss rate obtained prior to transition means the corrosion-dominant mass loss rate depending on solubility according to tested pH level. After transition, the mass loss rate is proportional to the kinetic energy of impinging droplets.

**Table A1. 1 Accumulated mass loss of LDIE accelerated tests for A106
Gr.B and A335 P22**

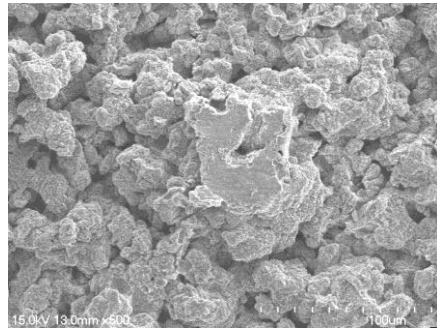
Test number	Date (yy/mm/dd)	test time (hr)	Accumulated mass loss(mg)							
			A106 Gr.B(specimen number a#)				A335 P22(specimen number #b)			
			a10	a11	a12	a13	b10	b11	b12	b13
Ex-1	13/06/14-13/06/20	24	37.09	36.81	37.14	37.11	29.26	29.06	29.09	28.79
		48	68.61	68.29	68.62	68.64	55.22	55.24	55.26	55.00
		72	222.13	238.75	243.81	221.69	118.68	109.28	134.27	124.99
		96	340.24	321.04	315.04	293.94	535.53	521.02	473.81	474.93
Ex-2	13/05/09-13/05/19	a14	a15	a16	a17	b14	b15	b16	b17	
		24	11.13	11.04	11.14	11.12	8.73	8.72	8.78	8.64
		48	25.39	25.27	25.39	25.40	20.45	20.45	20.43	20.35
		72	93.24	100.28	102.40	93.11	56.39	45.89	49.85	52.49
96	139.50	131.63	129.17	120.52	194.26	213.63	219.57	194.72		
Ex-3	13/07/24-13/08/10	a18	a19	a20	a21	b18	b19	b20	b21	
		24	0.29	0.28	0.32	0.28	0.04	0.04	0.04	0.05
		48	0.39	0.38	0.45	0.39	0.11	0.10	0.09	0.09
		72	0.69	0.72	0.72	0.71	0.13	0.11	0.10	0.10
96	0.85	0.89	0.92	0.88	0.15	0.12	0.12	0.14		
Ex-4	13/08/16-13/08/25	a22	a23	a24	a25	b22	b23	b24	b25	
		24	0.81	0.79	0.83	0.78	0.10	0.12	0.14	0.13
		48	1.15	1.12	1.17	1.10	0.24	0.27	0.25	0.25
		72	2.01	1.98	2.04	1.90	0.29	0.30	0.32	0.33
96	2.21	2.11	2.31	2.14	0.33	0.39	0.38	0.34		
Ex-5	14/09/09-14/09/17	a26	a27	a28	a29	b26	b27	b28	b29	
		24	3.11	3.08	3.19	3.14	5.59	5.89	5.05	5.31
		48	6.41	6.26	6.37	6.33	10.17	11.77	10.09	10.61
		72	9.61	9.23	9.56	9.24	16.76	17.66	15.14	15.92
96	12.81	12.31	12.74	12.05	24.34	23.54	20.18	21.22		
Ex-6	14/09/26-14/10/04	a30	a31	a32	a33	b30	b31	b32	b33	
		24	3.71	3.68	3.71	3.71	7.57	7.39	7.87	7.95
		48	6.86	6.83	6.86	6.86	14.98	14.64	15.59	15.76
		72	25.63	24.09	23.62	22.61	24.26	23.29	25.95	25.77
96	34.17	32.12	31.49	30.15	48.87	47.53	51.29	52.05		
Ex-7	13/06/22-13/07/02	a34	a35	a36	a37	b34	b35	b36	b37	
		24	21.14	20.98	21.17	21.15	16.67	16.56	16.58	16.41
		48	39.11	38.92	39.11	39.12	31.47	31.48	31.49	31.35
		72	126.54	136.08	138.97	126.36	67.64	72.28	77.53	71.24
96	221.76	230.26	231.97	221.63	309.31	320.58	324.54	321.82		
Ex-8	13/10/20-13/10/26	a38	a39	a40	a41	b38	b39	b40	b41	
		24	8.47	8.39	8.44	8.45	6.63	6.51	6.67	6.57
		48	19.31	19.21	19.38	19.29	15.54	15.51	15.53	15.47
		72	77.82	76.21	70.76	70.86	34.88	42.86	37.89	39.89
96	98.84	100.03	91.61	106.02	156.94	147.64	166.87	147.99		
Ex-9	13/10/27-13/11/02	a42	a43	a44	a45	b42	b43	b44	b45	
		24	16.07	15.94	16.09	16.07	12.67	12.59	12.60	12.47
		48	29.72	29.58	29.72	29.73	23.92	23.92	23.93	23.83
		72	96.17	103.42	105.62	96.03	51.41	54.93	58.92	54.14
96	167.53	175.00	176.30	168.44	243.64	241.47	250.76	245.75		
Ex-10	13/11/03-13/11/09	a46	a47	a48	a49	b46	b47	b48	b49	
		24	28.19	27.98	28.23	28.20	22.11	21.88	22.24	22.09
		48	52.14	51.92	52.15	52.17	42.00	41.80	41.97	41.98
		72	168.72	168.48	185.30	182.45	102.05	94.99	90.20	83.05
96	178.42	201.38	239.43	223.39	358.70	351.44	401.30	395.98		

A2. Microstructure images for LDIE damaged specimens

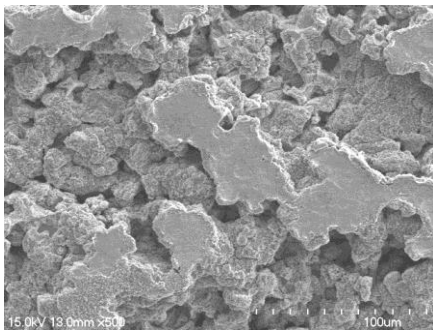
To investigate damage mechanism of LDIE, micro- and nano-structural analysis has been examined. Optical microscope, Normal SEM, FE-SEM, and FIB were adopted to clarify the details of damage mechanisms. The key factors influencing the LDIE damage rate have been identified as pH, droplet velocity, and droplet size. As shown in Table 4.2, the LDIE tests have been examined. From Figure A2.1 and Figure A2.2, it has been shown that the LDIE damage can be deepened in relatively lower pH conditions.



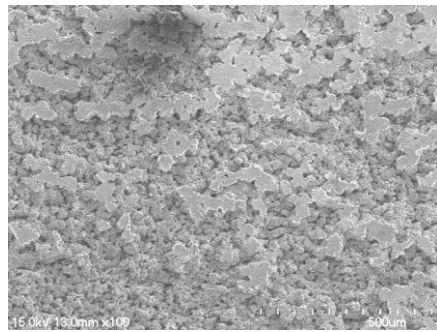
(a)Ex-1 (a10-96hr)



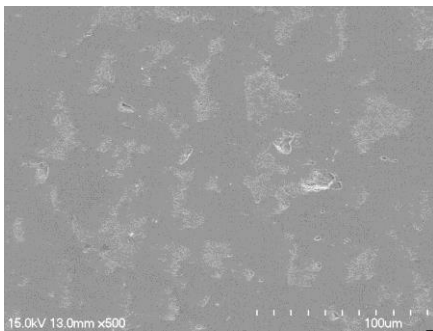
(b)Ex-1 (b10-96hr)



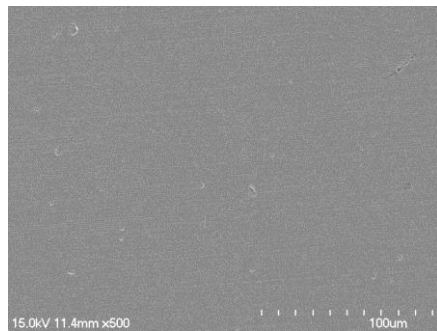
(c)Ex-2 (a16-96hr)



(d)Ex-2 (b12-96hr)

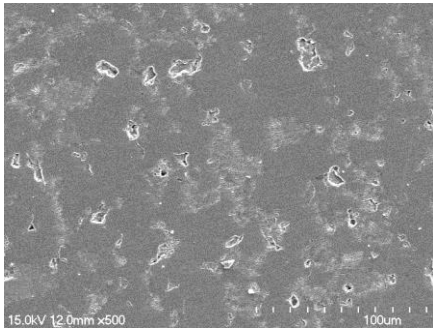


(e)Ex-3 (a19-96hr)

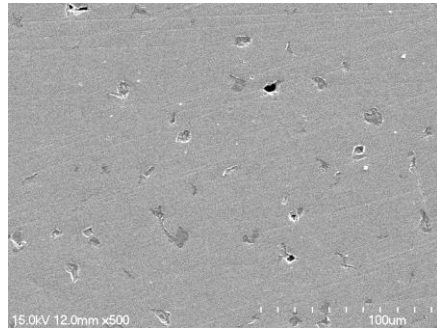


(f)Ex-3 (b20-96hr)

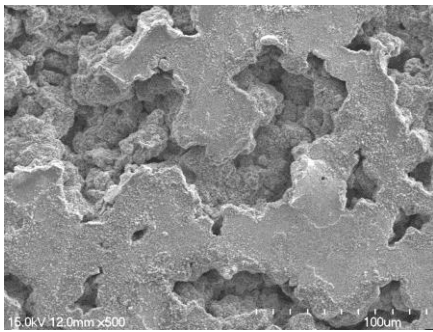
Figure A2. 1 SEM images for damaged specimens(Ex.1,2,3).



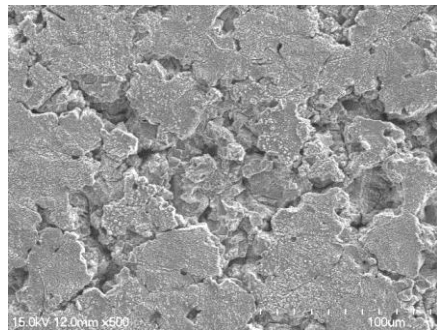
(a)Ex-4 (a24-96hr)



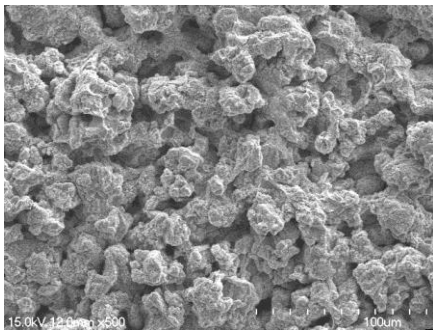
(b)Ex-4 (b23-96hr)



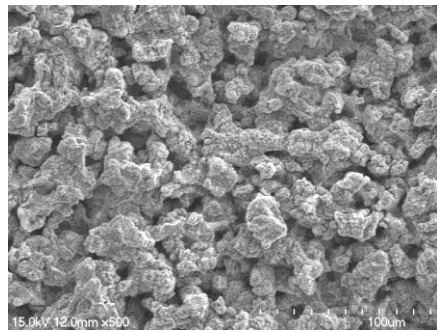
(c)Ex-6 (a31-96hr)



(d)Ex-6 (b33-96hr)



(e)Ex-10 (a48-96hr)



(f)Ex-10 (b49-96hr)

Figure A2. 2 SEM images for damaged specimens(Ex-4,6,10).

초 록

후쿠시마 사고 이후 가동중 원자력발전소에 대한 안전성 강화가 중요한 문제로 대두되고 있으며 이에 따라 설계수명을 넘어서는 기존 원자력 발전소의 계속 운전 평가가 안전성 측면에서 현안이 되고 있다. 장기 운전시 가동 원전의 안전성은 재료열화 현상에 대해 운전기간 동안 구조재의 건전성 확보 여부에 달려있다.

기존 재료 경년 열화 연구의 방향은 주로 PWR 1차 측 압력경계내의 구조재에 대해서 발생할 수 있는 문제에 초점이 맞춰져 있었다. 본 논문에서는 PWR 2차측의 저합금강의 액적충돌 침식(Liquid Droplet Impingement Erosion, LDIE)에 대하여 연구를 수행했다. 장기간 운전 및 정비 경험의 결과, 주로 저 합금강 배관소재로 구성되는 2차 측 배관계통에서 감육현상에 따른 파손 사례가 국내외에 지속적으로 보고되고 있으며, 해외의 경우 많은 인명 사상 사고가 발생했다. 이러한 배관 감육에 영향을 미치는 주요 현상으로 유동가속부식과 액적충돌침식이 그 원인으로 지목되고 있다.

특히 액적충돌침식에 의한 손상사례는 근래에 발생되고 있는 현상으로 국내외에 체계적인 연구가 전무한 실정이다. 따라서 발전소 운전환경에서 액적충돌침식 손상기구에 대한 연구가 절실하다. 관련연구의 어려움은 발전소환경에서 수십 년에 걸쳐 발생하는 현상을 실험실 환경에서 구현하기 어렵다는 점과 손상

영향인자에 의한 복합적인 상호작용으로 인해 손상 원인규명에 어려움이 있다.

그러므로, 손상기구 규명과 손상예측모델을 개발하기 위해서는 먼저 최대한 발전소 환경과 동일한 환경을 실험실에서 모사하도록 하되 배관감육의 진행을 실제 발전소 환경 하에서의 진행보다 가속화할 수 있는 실험장치를 개발하는 것이 중요할 것으로 판단되었다. 또한, 실제 발전소 환경에서는 부식의 진행을 최대한 억제하기 위해 pH를 높게(pH~9.2) 유지하지만, 이와 같은 배관감육 진행을 가속화하기 위해 pH를 통상적인 발전소 환경보다 낮게 조정하는 것이 효과적이라고 판단하였다. 또한 액적의 충돌로 인한 침식의 진행 역시 가속화하기 위해서는 액적속도 및 액적크기 역시 실제 발전소 환경에 비해 높이는 것이 바람직하다. 이에 따라, 액적충돌침식을 발생시키는 주요 손상영향인자로 생각되는 용존산소/수소, 온도, pH, 액적속도 및 액적크기 중, 용존산소/수소 및 온도의 경우는 발전소 환경과 동일하도록 하되 pH, 액적속도 및 액적크기를 제어하는 방식으로 본 연구를 진행하였다.

이에 따라, 실험수행을 위해 액적속도 및 액적크기를 제어할 수 있는 ASTM 표준시험법에 근거하되, pH를 제어할 수 있는 액적충돌 실험장치를 개발하였다. 즉, 실험분위기 chamber내에서 회전원판에 결속된 재료시편을 구동 축을 이용해 고속 회전시키고 상부의 액적 발생 노즐을 통해 균일한 분포의 밀도와 크기를 가지는 액적을 분사하여 충돌시키는 ASTM 표준시험법을 사용하였다. 고온에서 용존산소/소수 및 온도, pH가 제어된 화학수로 액적을 발생시키고 재순환 할 수 있는 특수한 손상실험모사장치를 개발하였다.

또한, 재료의 강도 및 합금원소비율 차이에 따라 부식 및 침식의 손상율이 다를 것으로 예상되는 저합금강 재료들 중, 배관 및 피팅재료로 일반적으로 사용되는 A106 Gr.B, A335 P22 저합금강 재료와 MnS의 영향을 조사하기 위해 SUM24L의 총 세 가지를 사용하였다.

즉, pH, 액적속도, 액적크기, 재료의 강도 및 합금원소비율 차이를 주요 손상영향인자로 하여 손상모사실험을 진행하였는데, 시간에 따른 누적 손상량 측정 결과 (i) 초기 손상율에 비해 손상율이 급격히 높아지는 transition time이 존재하며; (ii) transition time 시점 이전에는 표면손상이 존재함을 확인하였고, pH에 따라 동일 재료의 손상율이 상이하였으며; (iii) transition time 시점 이전에는 재료에 따른 손상율 차이가 상대적으로 미미하였으나 transition time 시점 이후에는 재료에 따른 손상율 차이가 상대적으로 큰 것으로 관찰되었다.

이와 같은 실험결과에 따라, 아래와 같은 손상기구에 대한 결론을 내렸다:

- (i) transition시점 이전, 즉 손상 초기단계에서는 부식이 손상발생원인으로 나타났다.
- (ii) transition시점 이후, 즉 손상 후기단계에서는 재료의 기계적인 물성(인장 강도 및 경도)에 따라 손상율이 상이하였으므로, 이 시점에서는 액적의 물리적인 충격에 의한 침식이 주요한 손상발생원인으로 나타났다.

이와 같은 손상기구학적 이해를 전제로, 추가적인 검증실험을 진행하였으며, 검증실험에 의해 (i) 초기에는 부식에 의해 재료의

펠라이트 조직 내에서 페라이트의 선택적인 용출에 의해 손상이 야기되며; (ii) 펠라이트 조직 내에서의 손상의 생성 및 성장을 통해 손상 표면의 roughness가 충분히 증가하면 액적의 물리적인 충격에 의해 표면이 떨어져 나가며, 이 때 손상률은 재료강도 및 경도의 영향을 받는 것으로 확인되었다.

따라서, 실험적으로 확인된 손상기구는 transition 시점을 경계로 하여 부식에 의한 손상이 지배적인 구간과 침식에 의한 손상이 지배적인 구간으로 나뉘며, 추가적인 분석 결과 transition point는 결정립 크기 정도의 깊이 방향 손상 시점으로 예측할 수 있다. 또한, 검증실험 결과를 바탕으로 하여 시간에 따른 손상 정도에 대해 bilinear prediction model을 개발하였으며 실험과의 오차를 평가하였다. 개발된 액적충돌침식 예측 모델을 원전 현장 손상사례와 비교 결과 30%의 오차 범위 내에서 결과가 일치함을 확인하였다.

주요어: 액적충돌침식, 저합금강, 가압경수로, 2차측 이상유동 손상기구, 가속화시험법
학 번: 2005-31016